

The Gaia-ESO Survey: Age-chemical-clock relations spatially resolved in the Galactic disc [★]

C. Viscasillas Vázquez^{1,2}, L. Magrini², G. Casali^{3,4}, G. Tautvaišienė¹, L. Spina⁵, M. Van der Swaelmen², S. Randich², T. Bensby⁶, A. Bragaglia⁴, E. Friel⁷, S. Feltzing⁶, G.G. Sacco², A. Turchi², F. Jiménez-Esteban⁸, V. D'Orazi⁵, E. Delgado-Mena⁹, Š. Mikolaitis¹, A. Drazdauskas¹, R. Minkevičiūtė¹, E. Stonkutė¹, V. Bagdonas¹, D. Montes¹⁰, G. Guiglion¹¹, M. Baratella¹¹, H. M. Tabernero¹², G. Gilmore¹³, E. Alfaro¹⁴, P. Francois¹⁵, A. Korn¹⁶, R. Smiljanic¹⁷, M. Bergemann¹⁸, E. Franciosini², A. Gonneau¹³, A. Hourihane¹³, C. C. Worley¹³, S. Zaggia⁵

(Affiliations can be found after the references)

Received 17 December 2021/ Accepted 25 January 2022

ABSTRACT

Context. The last decade has seen a revolution in our knowledge of the Galaxy thanks to the *Gaia* and asteroseismic space missions and the ground-based spectroscopic surveys.

Aims. To complete this picture, it is necessary to map the ages of its stellar populations. During recent years, the dependence on time of abundance ratios involving slow (s) neutron-capture and α elements (called chemical-clocks) has been used to provide estimates of stellar ages, usually in a limited volume close to the Sun. We aim to analyse the relations of chemical clocks in the Galactic disc extending the range to $R_{GC} \sim 6\text{--}20$ kpc.

Methods. Using the sixth internal data release of the *Gaia*-ESO survey, we calibrated several relations between stellar ages and abundance ratios $[s/\alpha]$ using a sample of open clusters, the largest one so far used with this aim (62 clusters). Thanks to their wide galactocentric coverage, we investigated the radial variations of the shape of these relations, confirming their non-universality.

Results. The multi-variate relations allowed us to infer stellar ages for field stars. We estimated our accuracy (ranging from 0.0 to -0.9 Gyr) and precision (from 0.4 to 2.3 Gyr) in recovering the global ages of open clusters, and the ages of their individual members. We applied the relations with the highest correlation coefficients to the field star population, finding an older population at lower metallicity and higher $[\alpha/Fe]$ in the thin disc, and a younger one at higher $[Fe/H]$ and low $[\alpha/Fe]$, as expected.

Conclusions. We confirm that there is no single age-chemical clock relationship valid for the whole disc, but that there is a dependence on the galactocentric position, which is related to the radial variation of the star formation history combined with the non-monotonic dependence on metallicity of the yields of the *s*-process elements from low- and intermediate-mass stars. Finally, the abundance ratios $[Ba/\alpha]$ are more sensitive to age than those with $[Y/\alpha]$ for young disc stars, and their slopes vary less with galactocentric distance. We remind the reader that the application of such relationships to field stars is only of statistical value.

Key words. Galaxy: abundances – Galaxy: disc – Galaxy: open clusters and associations: general – stars: abundances

1. Introduction

In the multi-dimensional space traced by *Gaia* (Gaia Collaboration et al. 2016, 2018, 2021) and the large, high-resolution spectroscopic surveys, such as *Gaia*-ESO (Gilmore et al. 2012; Randich et al. 2013), APOGEE (Majewski et al. 2017), and GALAH (De Silva et al. 2015), the missing variable is time, which can be traced by the ages of stars. However, stellar ages, as the other properties of stars, cannot be directly measured. They need a direct comparison with the outputs of stellar evolution models, through the so-called isochrone fitting, in which observed (colours and magnitudes) or derived (temperature and surface gravity) quantities are compared with theoretical values. Moreover, having both good models of stellar evolution and good observational measurements is not always sufficient to infer reliable age estimates, since isochrone fitting gives unsatisfactory results for field stars, particularly on the main sequence and the giant branch in of the Hertzsprung-Russel (HR) diagram, where the isochrones are particularly crowded. Therefore, in re-

cent years, alternative or complementary methods have been put in place to provide further estimates of stellar ages (see, e.g. Soderblom et al. 2014; Howes et al. 2019).

The first study, to our knowledge, to notice the net increase in the abundance of slow (s) neutron capture elements in young stellar populations is D'Orazi et al. (2009), in which the abundance of barium in young star clusters was seen to be higher than in the older ones. Maiorca et al. (2011, 2012) added a few more elements with important *s*-process contributions (yttrium, zirconium, lanthanum, and cerium), confirming the increasing trend towards younger ages. Subsequently, a number of works have attempted to both clarify the origin of this increase (see, e.g. Bisterzo et al. 2014; Mishenina et al. 2015; Trippella et al. 2016; Magrini et al. 2018; Spina et al. 2018; Busso et al. 2021) and to use their abundances to estimate the ages of stars, often using neutron capture *s*-process elements in combination with other elements with opposite behaviours, such as α elements – that we indicate as chemical clocks – and thus maximising the dependence of the relationship with age (see, e.g. Tucci Maia et al. 2016a; Nissen 2016; Feltzing et al. 2017; Fuhrmann et al. 2017; Slumstrup et al. 2017; Titarenko et al. 2019). Once the existence of a relationship between age and chemical clocks was established (see, e.g. Spina et al. 2016; Delgado Mena et al. 2019;

[★] Based on observations collected with the FLAMES instrument at VLT/UT2 telescope (Paranal Observatory, ESO, Chile), for the *Gaia*-ESO Large Public Spectroscopic Survey (188.B-3002, 193.B-0936, 197.B-1074).

Jofré et al. 2020), the next steps were the following: i) to clarify the applicability of these relationships with luminosity class (dwarf or giant) (see, e.g. Tucci Maia et al. 2016b; Slumstrup et al. 2017; Casamiquela et al. 2021), metallicity (see, e.g. Feltzing et al. 2017; Delgado Mena et al. 2019; Casali et al. 2020), and population type (thin disc, thick disc, halo) (see, e.g. Titarenko et al. 2019; Nissen et al. 2020; Tautvaišienė et al. 2021), or even in dwarf galaxies (Skúladóttir et al. 2019); ii) to calibrate them with a sample of stars with reliable age determination, which are usually open star clusters (OCs), solar twins, or targets with asteroseismic observations. Finally, it is essential to understand whether these relationships are valid throughout the Galactic disc, or whether they are necessarily position-dependent. For the first time, Casali et al. (2020) applied the relations derived from a large sample of solar-like stars located in the solar neighbourhood and noted that they fail to reproduce the ages of star clusters in the inner disc. They concluded that the relationship between age and chemical clocks is not universal and that it varies with galactocentric position. Later, Magrini et al. (2021b) suggested that the differences in the relationships between age and chemical clocks in different parts of the Galactic disc are due to the strong dependence on the metallicity of the yields of low-mass stars, which produce *s*-process elements during the final stages of their evolution. Casamiquela et al. (2021) used red clump stars in open clusters to investigate the age dependence of several abundance ratios, including those that contain *s*-process and α elements. They found that the relationship between $[Y/Mg]$ and ages outlined by open clusters is similar to the one found using solar twins in the solar neighbourhood. They also found that the abundance ratios involving Ba are those with the highest correlation with age. However, they also note that as one moves away from the solar neighbourhood, the dispersion increases and is in agreement with the findings of Casali et al. (2020), which attributed this to the spatial variation of the star formation history along the galactocentric radius.

In the present paper, we discuss the radial variation of the relations between ages and chemical clocks using the largest sample of open clusters so far used for this purpose: 62 OCs observed by the *Gaia*-ESO survey sixth internal release, *DR6*, which includes science clusters, calibration clusters, and archive clusters, that is those which were not observed by *Gaia*-ESO but were present in the ESO archive and then homogeneously re-analysed by the *Gaia*-ESO consortium. The paper is structured as follows. In Section 2, we describe the *Gaia*-ESO database and the solar-scale normalisation, while in Section 3 we depict our samples of member stars in open clusters and of field stars. In Section 4, we describe the relationships between $[El/Fe]$ and age and between the chemical clocks and ages, using open star clusters as calibrators. We also estimate the role of migration in determining such relations. We apply our relations to cluster stars (Section 5) and to field stars (Section 6). In Section 7, we discuss our results and provide our conclusions.

2. Data reduction and analysis

2.1. The *Gaia*-ESO *DR6*

We used data from *DR6* of the *Gaia*-ESO Survey obtained from the spectral analysis from the UVES spectra (resolving power $R=47,000$ and spectral range 480.0–680.0 nm). The spectra were reduced and analysed by the *Gaia*-ESO consortium, and the data analysis is organised in different working groups (WGs). The spectra are analysed with several pipelines, internally combined by each WG, and then the results from the different WGs

are homogenised using a database of calibrators, such as benchmark stars and open or globular clusters selected following the calibration strategy by Pancino et al. (2017) and adopted for the homogenisation by WG15 (Hourihane et al. in preparation). The data reduction, radial and rotational velocity determinations are undertaken in INAF-Arcetri (Sacco et al. 2014) using the FLAMES-UVES ESO public pipeline. The analysis process for the UVES spectra of F, G, and K stars in the field of the Milky Way (MW), in open clusters, and in calibration targets, including globular clusters, was described in Smiljanic et al. (2014).

The recommended parameters and abundances are distributed in the *DR6* catalogue, which includes those used in the present work: atmospheric stellar parameters, such as effective temperature, T_{eff} , surface gravity, $\log g$, and metallicity, $[Fe/H]$, and abundances of 32 elements, several of them in their neutral and ionised forms. In the present paper, we discuss the abundances of five *s*-processes, four α elements, and an odd-Z element. All the abundances (by number) are expressed in their usual logarithmic form: $A(El)=12+\log(n(El)/n(H))$, while the abundances normalised to the solar scale are indicated with $[El/H]=\log(n(El)/n(H))-\log(n(El)/n(H))_{\odot}$.

2.2. Solar abundance scale

In Table 1, we show, for the elements used throughout this work, both the solar abundances derived for the Sun in *Gaia*-ESO *DR6* and those from Grevesse et al. (2007), which are used in *Gaia*-ESO to build up both the model atmospheres and the synthetic spectra used by the consortium. We also include the average abundances of M67, which has a chemical composition very similar to the solar one (see, e.g. Önehag et al. 2011; Liu et al. 2016), and the abundances of their giant and dwarf member stars observed in *Gaia*-ESO *DR6*. We separate dwarf and giant stars in M 67 on the basis of their surface gravity: we define a giant star if $\log g < 3.5$, and a dwarf star if $\log g \geq 3.5$. In the first part of Table 1, we present the adopted α and odd-Z elements, namely Mg, Al, Si, Ca, and Ti. In the second part, we show the slow neutron-capture elements (Y, Zr, Ba, La, Ce). The agreement between the solar and the average M67 *Gaia*-ESO abundances, and those of Grevesse et al. (2007), is very good, within $1-\sigma$. In the last two columns, we show the abundances of the giant and dwarf members of M67 separately, to estimate the impact of a single set of normalising values to both giant and dwarf stars. Bertelli Motta et al. (2018) investigated variations in the surface chemical composition of member stars of M67 as a possible consequence of atomic diffusion, which takes place during the main-sequence (MS) phase (see, e.g. Bertelli Motta et al. 2017; Souto et al. 2019). They found that the abundances of MS stars differ with respect to those of the giant stars, consistently with the predictions of stellar evolutionary models. In our sample, these differences and other possible effects due to spectral analysis are also noted on the average values of M67 dwarfs and giants, in particular for Al, and for Si among the odd-Z and α -elements and Y among the neutron capture.

Although these variations are not very large, they can affect our comparison between giant stars (essentially cluster members) and dwarf stars (most of them composing the field star sample), modifying their abundance scale. We thus normalised the abundances of dwarf and giant stars using two different values, corresponding to average values of M67 for dwarf and giant stars (fifth and sixth columns of Table 1).

Table 1: iDR6 solar and M67 abundances for neutron-capture elements and α -elements.

A(El)	Sun (iDR6)	Sun Grevesse et al. (2007)	M67 (iDR6)	M67 (iDR6) (giants)	M67 (iDR6) (dwarfs)
Mg I	7.51 \pm 0.02	7.53 \pm 0.09	7.50 \pm 0.04	7.53 \pm 0.04	7.49 \pm 0.04
Al I	6.40 \pm 0.02	6.37 \pm 0.06	6.42 \pm 0.03	6.49 \pm 0.03	6.39 \pm 0.03
Si I	7.44 \pm 0.02	7.51 \pm 0.04	7.44 \pm 0.03	7.50 \pm 0.02	7.41 \pm 0.02
Ca I	6.32 \pm 0.02	6.31 \pm 0.04	6.26 \pm 0.02	6.25 \pm 0.02	6.29 \pm 0.03
Ti I	4.89 \pm 0.02	4.90 \pm 0.06	4.90 \pm 0.03	4.87 \pm 0.03	4.91 \pm 0.03
Y II	2.19 \pm 0.04	2.21 \pm 0.02	2.17 \pm 0.04	2.09 \pm 0.02	2.21 \pm 0.05
Zr I	2.62 \pm 0.13	2.58 \pm 0.02	2.54 \pm 0.02	2.51 \pm 0.03	2.61 \pm 0.02
Ba II	2.20 \pm 0.04	2.17 \pm 0.07	2.17 \pm 0.06	2.12 \pm 0.07	2.19 \pm 0.06
La II	1.13 \pm 0.02	1.13 \pm 0.05	1.17 \pm 0.07	1.17 \pm 0.02	1.17 \pm 0.09
Ce II	1.70 \pm 0.02	1.70 \pm 0.10	1.66 \pm 0.07	1.66 \pm 0.03	1.67 \pm 0.09

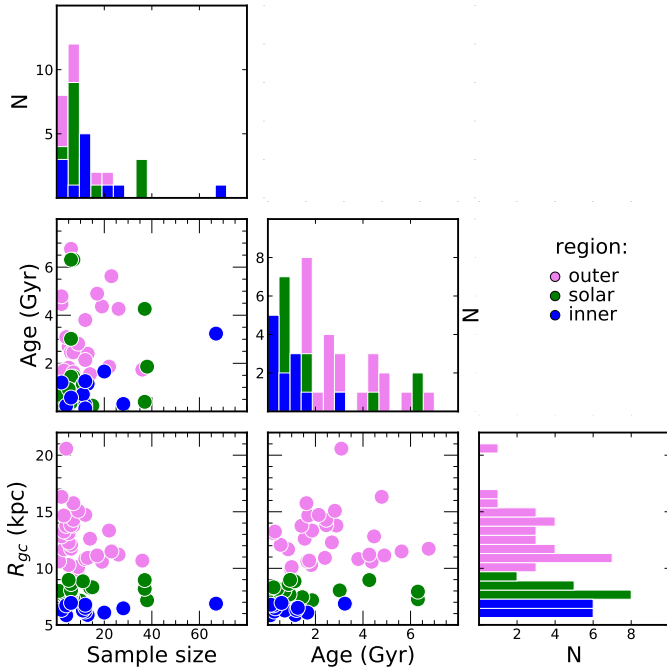


Fig. 1: Distributions of ages, galactocentric distances, and sizes (number of observed members in DR6) for our sample of clusters colour-coded by R_{GC} (inner disc $R_{GC} < 7$ kpc in blue; solar region $7 \text{ kpc} < R_{GC} < 9$ kpc in green; outer disc $R_{GC} > 9$ kpc in pink).

3. Samples

The sample of WG 11 stars in DR6 is made up of 6877 stars (column 'WG' in the *Gaia*-ESO nomenclature), of which 3613 are Galactic field stars, 2794 are classified as star cluster candidates, spread over 96 (both globular and open) clusters, and 470 are standard field stars, including benchmark stars and asteroseismic fields. We divided our sample into two sets, the first containing only members of clusters older than 100 Myr, and the second containing the field stars. We used the first sample to calibrate the relations between age, galactocentric distance, R_{GC} , and abundance ratios, while the second sample was used to cross-check the applicability of our method.

3.1. Sample of member stars of open clusters

Open clusters are among the best calibrators between the properties of stars and their ages. The member stars of the same cluster show homogeneity in age and chemical composition for most elements (exceptions are those processed within the nuclear region of the star and brought to the surface by convection during the evolved phases of giants such as C, N, and Li; see, e.g. Randich & Magrini 2021) and within the effect related to a secondary process such as atomic diffusion.

In the present work, we considered 62 OCs with age ≥ 100 Myr, which contain a total number of 788 member stars. Among the cluster members, we only considered those that have at least one abundance value of an s process and of one of the considered α - or odd- Z elements, which reduced our sample to 716 stars. The analysis of younger clusters should be specific, as detailed in Baratella et al. (2020, 2021), and the determination of their abundances are affected by activity, rotation, and problems in the derivation of the microturbulent velocity, ξ . For this reason, they were not included in this work. For our sample clusters, we adopted ages and galactocentric distances from the homogeneous analysis with *Gaia* DR2 data of Cantat-Gaudin et al. (2020). In Figure 1, we show the distributions of their number of observed member stars (sample size), age, and R_{GC} . Since we only used the UVES data, for most clusters we have about ten members, but in some cases there are more. The ages range from 100 Myr to about 7 Gyr, while the R_{GC} from about 6 kpc to 20 kpc. An interesting aspect of the open cluster sample is the absence of clusters older than about 3 Gyr in the inner disc. A comparison with the age distribution in the same three radial intervals used in our work of the whole cluster sample in Cantat-Gaudin et al. (2020) clearly shows the same effect: an almost total absence of old clusters in the inner disc, as shown in Figure 2. The limitation is likely intrinsic, due to the higher efficiency of destructive processes in higher density areas, as recently observed in M51. Messa et al. (2018) found that the age distribution of clusters is dependent on the region considered and is consistent with rapid disruption only in dense regions, while little disruption is observed at large galactocentric distances and in the inter-arm region.

This lack of inner old clusters has significant consequences on our calibration work, because it will not allow us to date the oldest stars in the inner disc unless we accept extrapolations of the relationships.

The membership and the corresponding probability are computed in different ways depending on how many stars are observed in each cluster. For 41 clusters (676 stars), we used the membership analysis described in Jackson et al. (2022), and for

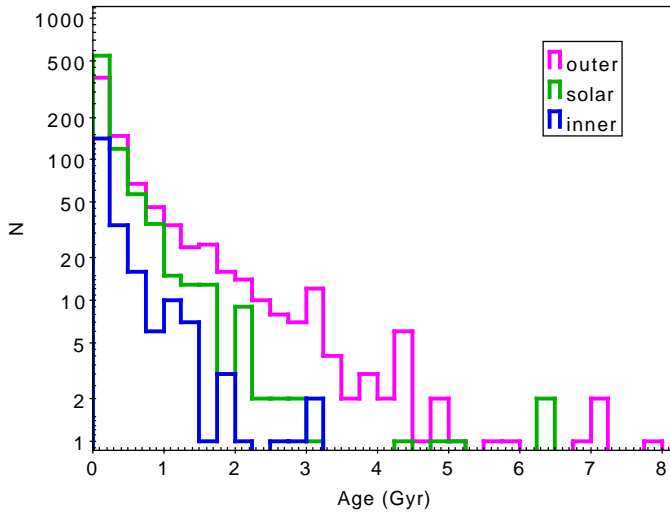


Fig. 2: Distributions of ages in the three radial bins for the sample of 1017 open star clusters of Cantat-Gaudin et al. (2020). The histograms are colour-coded by R_{GC} (inner disc $R_{GC} < 7$ kpc in blue; solar region $7 \text{ kpc} < R_{GC} < 9$ kpc in green; outer disc $R_{GC} > 9$ kpc in pink).

the remaining clusters we used the analysis of Magrini et al. (2021a). The former used a maximum likelihood technique to determine membership probabilities for each star based on their 3D kinematics, combining the parameters of *Gaia*-ESO with *Gaia* DR3, 2MASS, and VISTA. Using the membership of Jackson et al. (2022), we only included members with probability > 0.9 (MEM3D). For the other clusters, following Magrini et al. (2021a), the selection of members was done in two different ways according to the number of observed candidate stars. When the cluster had more than 20 potential member stars, the selection was done by performing a simultaneous fit of the *Gaia*-ESO radial velocities, RVs, and the parallaxes and proper motions from *Gaia* DR3 (Gaia Collaboration et al. 2021). When the cluster had fewer than 20 potential member stars, the authors derived the peak and standard deviation of the RV distribution and selected stars within 2σ of the peak, then computing the average parallax, proper motion, and their standard deviations, and excluding those differing by more than 2σ from the average values.

Since the median signal-to-noise ratio (S/N) of the cluster member stars ($< S/N \sim 100$) is higher than that of field stars, and since we did not use individual abundances of member stars for clusters, but we adopted average values from all members, we did not apply any selection criteria based on the S/N or errors in parameters. We only discarded some stars with high errors in abundance of neutron capture elements (error in abundance ≥ 0.1 dex). In addition, for each cluster, we used the interquartile range rule to detect potential outliers that fall outside of the overall abundance pattern. This range is defined by $(Q1 - 1.5 \times IQR, Q3 + 1.5 \times IQR)$, where IQR is the difference between the 75th and 25th percentiles of the data, being Q1 the lower quartile, Q2 the median, and Q3 the upper quartile (see Figure A.1 in which the outlier stars stand out from the main distribution for each cluster).

We examined the outliers for each cluster individually and in the context of the entire data set, finding some stars with anomalous abundances, in several cases in extreme abundance of s-process elements (e.g. 07465200-0441557 in Berkeley 39, with

differences above 4σ for [Y/H] and [Ba/H], 06025078+1030280 in NGC2141, and 06071407+2406547 in NGC2158, where those IDs are the CNames given in the *Gaia*-ESO survey). The exclusion of out of range stars (26 stars that are outliers in more than one s-process element) in addition to the reduction of the scatter improves the correlations. These stars will be analysed in detail in a future work, in which the overabundance of s-elements will be correlated with stellar properties, including binarity and rotation.

In Table 1 of the appendix, we provide the global metallicity of each cluster from Randich et al. (2022), together with R_{GC} and age (Cantat-Gaudin et al. 2020), and the abundance ratios used along the paper. We provide both [El/H] and [El/Fe] because the transition between the two ratios is not straightforward, as they are calculated star by star and then averaged, while the overall metallicity [Fe/H] is generally calculated with a larger number of members.

3.2. Sample of field stars

Our set of field stars is composed of two sub-samples: i) 4083 MW field stars, which include the stars observed in the *Gaia*-ESO field samples by selecting the GES_FLD keywords related to the field stars (GES_MW for general Milky Way fields, GES_MW_BL for fields in the direction of the Galactic bulge, GES_K2 for stars observed in Kepler2 (K2) fields, GES_CR for stars observed in CoRoT fields), and benchmark stars GES_SD and ii) 385 field stars that are non-members of open clusters (age > 100 Myr), as described in Section 3.1.

We combined the two samples of field stars, performing a further selection on stellar parameter uncertainties: $S/N > 20$; $eT_{\text{eff}} < 150$ K, $e \log g < 0.25$, $e[\text{Fe}/\text{H}] < 0.20$, and $e\xi < 0.20 \text{ km s}^{-1}$. We also applied a further cut in abundance errors, considering only those values that have an $eA(EI) < 0.1$. Our quality selection reduces the total number of MW field stars from 4468 to 3975, with a median $S/N \sim 74$.

The selected sample of 3975 stars is made up of 711 stars (18%) with $\log g \leq 3.5$ (giant stars) and 3264 stars (82%) with $\log g > 3.5$ (dwarf stars). Of these 3975 stars, 19% are located in the inner disc, 78% are in the solar region and 3% belong to the outer disc. Due to the selection function adopted in the *Gaia*-ESO survey for UVES observations (see Stonkutė et al. 2016), the field population is dominated by stars at the main sequence turn-off (MSTO), while several giant stars are present that are non-members of open clusters.

4. Relations between age, R_{GC} , and abundance ratios in open clusters

4.1. Age versus [El/Fe] relations

The relation between the abundances of neutron-capture elements and stellar ages has been widely investigated (e.g. D’Orazi et al. 2009; Maiorca et al. 2011, 2012; Yong et al. 2012; Mishenina et al. 2013b,a; Jacobson & Friel 2013; Battistini & Bensby 2016; Marsakov et al. 2016; Nissen 2016; Reddy & Lambert 2017; Delgado Mena et al. 2017; Spina et al. 2018; Magrini et al. 2018; Tautvaišienė et al. 2021; Casamiquela et al. 2021; Baratella et al. 2021; Zinn et al. 2021; Sales-Silva et al. 2021). However, most of the previous works were limited to the solar neighbourhood region, using both solar twins or star clusters. Exceptions are the works of Magrini et al. (2018), which is based on a sample of open clusters from *Gaia*-ESO DR5, about 20 clusters located at various galactocentric distances, and the very re-

cent work of Sales-Silva et al. (2021), in which a sample of 42 clusters from the APOGEE survey was used to investigate the spatial variation of the relation $[\text{Ce}/\alpha]$ versus age, finding that is not the same across the Galactic disc. This is possibly due to the dependence of AGB yields on metallicity.

Unlike previous studies, our sample offers the unique advantage of having a very large sample of OCs (62 objects) with homogeneously derived abundances of neutron-capture elements, covering a wide range of ages and galactocentric distances (see Fig. 1). This allows us to study the relationships between ages and abundance ratios in a spatially resolved way and to derive them at various galactocentric distances. We divided our sample clusters in three galactocentric regions: an outer region, which includes 30 OCs located at $R_{gc} > 9$ kpc; a central region, where our Sun is located, includes 20 OCs at $7 \leq R_{gc} \leq 9$ kpc; and an inner region, comprising 12 OCs at $R_{gc} < 7$ kpc.

In Fig. 3, we show the variation of $[\text{El}/\text{Fe}]$ as a function of $[\text{Fe}/\text{H}]$ and of age. In the left panels, we observe important differences in the clusters belonging to the three regions mentioned above. The clusters in the outer disc are generally more metal poor than the clusters in the inner disc and in the solar neighbourhood, while the differences in $[\text{El}/\text{Fe}]$ are less pronounced. Typically, outer disc clusters have $[\text{El}/\text{Fe}] > 0$, while the inner disc ones have $[\text{El}/\text{Fe}]$ solar or sub-solar. The results are more clear when looking at the right panels, in which $[\text{El}/\text{Fe}]$ are shown as a function of the cluster age; for all the elements, $[\text{El}/\text{Fe}]$ are underabundant for a given age in the inner disc with respect to those of the outermost regions. For all three regions, we observe an increasing trend of $[\text{El}/\text{Fe}]$, confirming previous literature results. $[\text{Ba}/\text{Fe}]$, as noted in the past (e.g. D’Orazi et al. 2009; Maiorca et al. 2012; Mishenina et al. 2015), has the strongest upward trend.

In Fig. 4, we show the results of the coefficients of the weighted regressions (WLS) in the three regions in the following form: $[s/\text{Fe}] = m \cdot \text{Age} + c$. As a weight, we apply the expression:

$$\frac{1}{\left(\frac{\sigma}{\sqrt{N}}\right)^2},$$

where σ is the standard deviation of the abundance ratios for the member stars of every cluster, and N is the number of member stars with values of the corresponding abundance ratio. The coefficients are reported in Table A.2 together with the Pearson correlation coefficients (PCCs).

We note the different behaviour of the first-peak elements (Y and Zr) with respect to the second-peak ones (Ba, La, Ce), the former having lower intercept values than the latter. For all s -process-dominated elements, the slope of the regression is steeper in the inner disc than in the other two regions, while the value at the intercept, $[\text{El}/\text{Fe}]$, is lower in that region (see Fig. 4). In Table 2 of the appendix, we provide the coefficients of the weighted linear fits for the three radial regions.

In the work of D’Orazi et al. (2009), the $[\text{Ba}/\text{Fe}]$ ratio was found to dramatically increase at decreasing ages, with very high growth in very young stars. As discussed in Baratella et al. (2021), the higher enhancement of $[\text{Ba}/\text{Fe}]$ with respect to $[\text{La}/\text{Fe}]$ and $[\text{Ce}/\text{Fe}]$ in young stars cannot be easily explained, either with non-local thermodynamic equilibrium (NLTE) effects or with stellar nucleosynthesis and chemical evolution models. To look for a plausible explanation, they explored different scenarios related to the formation and behaviour of spectral lines, from the dependence on the different ionisation stages and the sensitivity to the presence of magnetic fields and the effect of stellar activity. However, all these effects cannot fully explain

the different behaviour of Ba in young stars. In our sample, we considered clusters older than 100 Myr; thus, we expect a relatively smaller difference between Ba, and the other elements of the second peak. However, as mentioned above, Figures 3 and 4 show that there are some differences among these elements, as already found in Magrini et al. (2018). Following Mishenina et al. (2015), other possible explanations are related to some extra production of Ba via an intermediate neutron-capture process, the so-called i -process, triggered by the mixing or ingestion of H in He-burning stellar layers (Cowan & Rose 1977; Bertolli et al. 2013). To summarise, though the origin of the $[\text{Ba}/\text{Fe}]$ increase in young stars does not have a complete theoretical explanation, the large slope of the $[\text{Ba}/\text{Fe}]$ age relation makes Ba an excellent age proxy, at least for ages above 150 Myr (see Spina et al. 2020; Baratella et al. 2021).

4.2. Age versus $[s/\alpha]$ relations: Chemical clocks across the disc

The idea of combining pairs of elements with different origins, particularly s processes and α elements (or odd-Z elements such as Al), has taken shape in the last decade (see, e.g. Tucci Maia et al. 2016a; Nissen 2016; Feltzing et al. 2017; Fuhrmann et al. 2017; Slumstrup et al. 2017; Titarenko et al. 2019; Casali et al. 2020). The combination of the abundances of an s -process element with other elements with opposite behaviour, such as α elements, maximise their correlation with stellar age. Several relations have been established and calibrated in the solar neighbourhood (see, e.g. Spina et al. 2016; Delgado Mena et al. 2019; Jofré et al. 2020; Tautvaišienė et al. 2021). Here, we aim to extend them in different regions of the Galactic disc using our sample of open clusters. For each neutron-capture peak, we selected the element with the highest percentage from an s process in the Sun (see, e.g. Arlandini et al. 1999; Bisterzo et al. 2014): Y for the first peak and Ba for the second one. We combined them with several α elements, namely Mg, Si, Ca and Ti, and Al (which can be also considered an odd-Z element, but has a behaviour very similar to the other α elements).

To find the best way to describe the relations between the age of the clusters and their chemical characteristics, we used multilinear weighted regressions that take into account age, metallicity, and R_{GC} , in the following form: $[s/\alpha] = m_1 \cdot \text{Age} + m_2 \cdot R_{GC} + m_3 \cdot [\text{Fe}/\text{H}] + c$. A similar approach was used in the work of Casali et al. (2020), who took into account $[\text{Fe}/\text{H}]$ in their sample of solar-like stars. We computed both a global regression, considering all clusters in the sample, and individual regressions for each radial region. For all regressions, we adopted the same weight system, as described in Section 4.1. In Table A.3, we report the coefficients of the weighted multivariate regressions for the three radial regions, and for the global sample including all clusters at all R_{GC} .

In Fig. 5, we plot $[\text{Y}/\alpha]$ and $[\text{Ba}/\alpha]$ versus cluster ages in the three regions of the Galactic disc, as defined above. Here, and in the following sections, we simplify our workings by including Al in the group of α elements, and thus when referring to $[s/\alpha]$, we also consider Al. In the left panels of Fig. 5, we find well differentiated behaviours; in the outer and central regions, we have decreasing trends of $[\text{Y}/\alpha]$ with increasing age, while in the inner region we observe a reverse trend. This was already noted, with a smaller sample size, in Magrini et al. (2021b). In the right panels of Fig. 5, the abundance ratios containing Ba and an α element show a decreasing trend with increasing age in all three regions. In addition, the innermost region shows a stronger trend than the others, with a steeper slope.

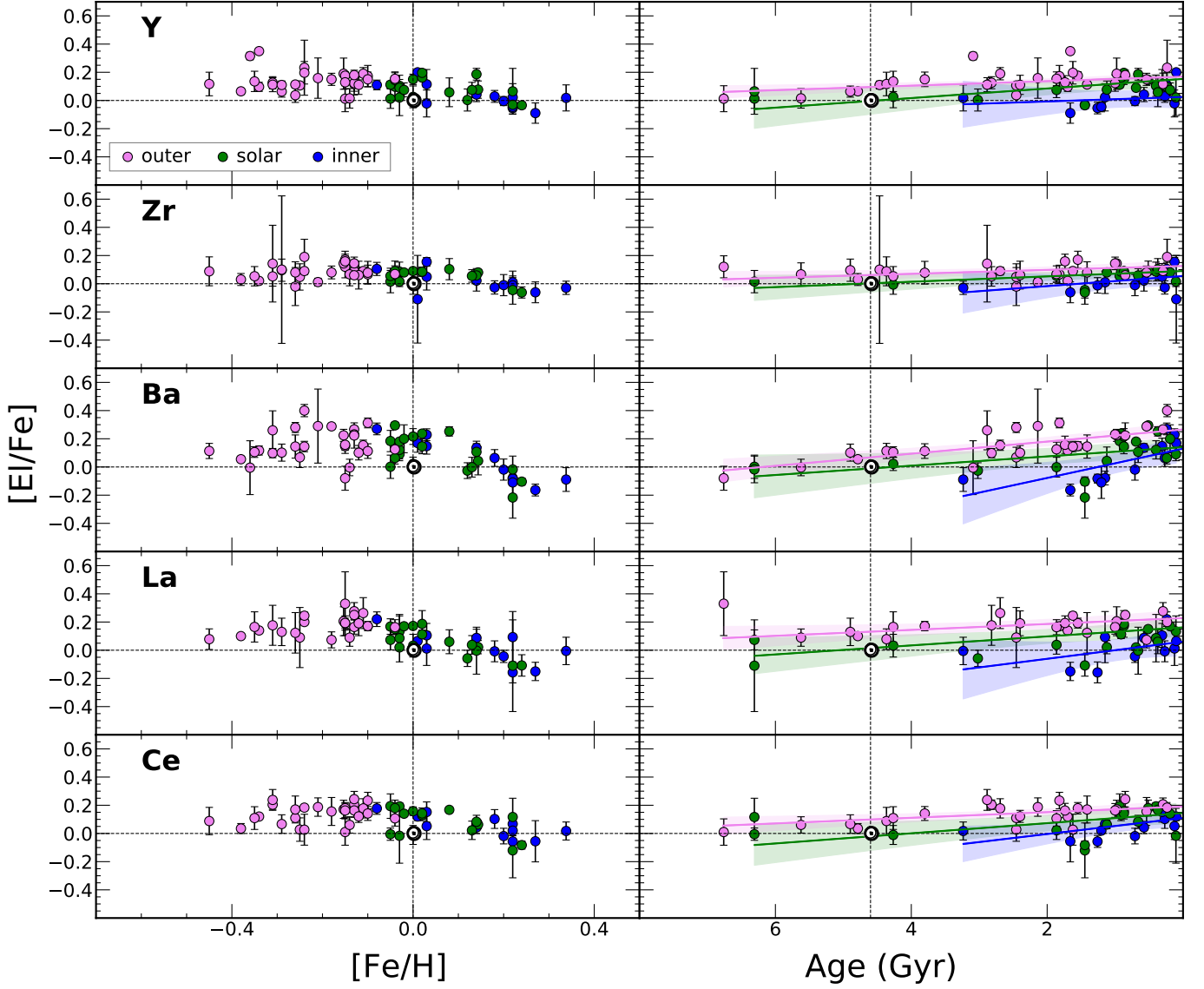


Fig. 3: $[El/Fe]$ versus metallicity and age. In the left panels, we show $[Fe/H]$ versus $[El/Fe]$, and in the right panels we show age versus $[El/Fe]$ for our sample of OCs divided into the three galactocentric regions. In blue, we show the OCs located in the inner disc, in green we show those located in the solar neighbourhood, and in pink we show the ones located in the outer disc. In the right panels, the continuous lines are the univariate linear regressions (one for each radial region, colour-coded according to the corresponding sample of OCs), while the shaded regions are their confidence intervals.

The coefficients (m_1 , m_2 , m_3 and c), and the correlation coefficients are also shown in Fig. 6, in which we separate the abundance ratios with Y and with Ba, for each radial region and for the whole sample. It is interesting to notice that the region that differs the most from the others is the inner region, while that around the Sun and the outer region are very similar, and even similar to the global relationship. Therefore, the multivariate regression computed with the whole sample of clusters might still be a good approximation for the solar neighbourhood and the outer region, while it fails to reproduce the inner disc region (cf. Casali et al. 2020).

4.3. Role of migration in open clusters

Radial migration plays an important role in the redistribution of stellar populations, particularly the older ones, in our Galaxy.

What weight migration holds in shaping the spatial distribution of more massive populations such as clusters, with respect to single stars, is not yet settled (see, e.g. Anders et al. 2017; Chen & Zhao 2020; Zhang et al. 2021; Netopil et al. 2021). To estimate the possible effect of radial migration in our relationships, we calculated the orbits of our cluster sample using the GALPY code, with the axis-symmetric potential MWPOTENTIAL2014 (Bovy 2015). We adopted the guiding radius (R_g , defined as the average between the minimum and maximum radius, see, e.g. Halle et al. 2015) instead of their present time R_{GC} to recompute the relations between age and abundance ratios, associating the clusters with the three radial regions on the basis of their R_g . Adopting R_g can indeed mitigate the effect of blurring due to epicyclic oscillations around the guiding radius (Schönrich & Binney 2009), while it cannot overcome the migrating effect of churning, that is the change of R_g due to in-

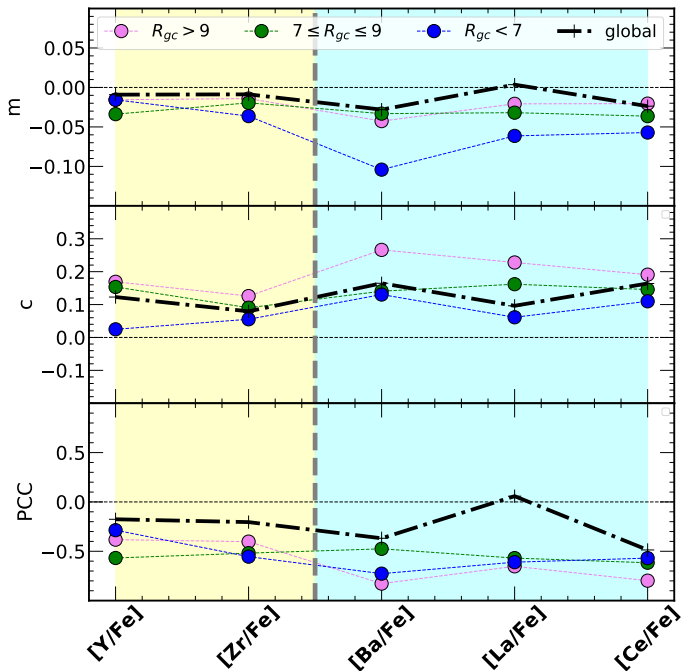


Fig. 4: Weighted regression coefficients for the age versus $[E/Fe]$ relation of 62 OCs by R_{GC} . The yellow area corresponds to the elements of the first s -process peak (Y and Zr), and the cyan area corresponds to those of the second peak (Ba, La and Ce). In the upper panel, we show the slope in dex Gyr^{-1} of the relations. In the central panel, we present the value of the intercept (dex), while in the bottom panel we see the correlation coefficient. In all panels, we use the following symbols: blue circles for the inner region, green circles for the solar region, pink circles for the outer region, and dashed black lines for the whole sample.

teractions with a lasting non-axisymmetric pattern such as long-lived spiral arms or long-lived bars (Sellwood & Binney 2002; Binney & Tremaine 2008). Using R_g , we found a new redistribution in the three regions: eight clusters might be visitors in their respective, initially assigned regions. The most affected region is the inner disc, which is repopulated with seven clusters coming mostly from the central region of the disc, with the exception of one cluster coming from the outer region (ESO 92 05). The outer disc is less affected by redistribution. The other seven clusters that move from the solar region to the inner region are NGC6791, Berkeley 44, NGC6802, NGC4815, Trumpler 20, NGC4337, and Collinder 261. Among them, NGC6791, which is both old and metal rich, is known to have a high probability of being a migrator (cf. Jílková et al. 2012; Netopil et al. 2021). Taking into account the effect of blurring, the regions are redistributed to contain 20 OCs in the inner disc instead of 7; 13 in the solar region instead of 20; and 29 in the outer region instead of 30.

We recalculated the relations adopting R_g instead of R_{GC} . As expected, only regressions for the inner and solar regions change when replacing R_{GC} with R_g . There is not an improvement in the quality of the fits, with a decrease in the correlation coefficients in the inner disc and in the solar neighbourhood (about 0.1 lower than those obtained with R_{GC}). In the next sections, we use the relationships obtained with the current galactocentric position.

4.4. Comparison with literature results

In this section, we compare our results with three recent literature works (Casali et al. 2020; Jofré et al. 2020; Casamiquela et al. 2021). In Fig. 7, we show the coefficient m_1 related to *age* and computed for the samples of open clusters in the outer and solar regions with the results from Casali et al. (2020) (yellow dots) for a sample of solar-like stars (and later applied to open clusters), those of Casamiquela et al. (2021) for two samples of open clusters (divided and closer than 1 kpc to the Sun and more distant; red dots and triangles respectively), and those of Jofré et al. (2020) for a sample of 80 solar twins (cyan dots in Fig. 7). The samples of solar twins or solar-like stars are to be compared with our sample of clusters in the solar region, while our outer disc sample can be compared with the outermost sample of Casamiquela et al. (2021). The general agreement is very good, and our slopes for the solar region sample agree well with the solar-like stars from different authors. The largest differences are seen in a sample of Casamiquela et al. (2021) for $[Ba/Ca]$ and $[Ba/Ti]$, which might be related to the inclusion of younger clusters in their sample.

5. Application to cluster stars

5.1. Global ages of open clusters

The first step in verifying the validity of our relations and their ability to provide a reliable estimate for the stellar ages is to reapply the same relations to clusters, by comparing the input ages from isochrone fitting with those obtained from the ten considered chemical clocks. The comparison between the two ages is shown in Fig. 8. The cluster ages, for each range of R_{GC} , are computed with the corresponding radial relations or with the global relations (throughout the entire R_{GC} interval). In the panels in each row, we show the results for a given chemical clock. There are three main aspects to note: *i*) the scatter increases for younger ages for almost all relations, *ii*) some relations allow us to recover the input ages with greater accuracy (closer to the 1-to-1 relation) and precision (less scatter) than the others. We defined our accuracy as the mean average difference between input and output ages obtained from our relations (which is indeed a sort of mean bias with respect to the reference values), while the precision (which can be considered as the scatter or internal error calibration) is the standard deviation of the mean difference; *iii*) the global relations generally produce worst results, especially for the younger ages (which is expected, since younger clusters dominate the inner region, for which the global relations do not work). The accuracy and precision, as defined above, for all radial bins, including the global one, and for all the considered abundance ratios are shown in Table 2.

The best set of relations, in terms of both accuracy, precision, and recovering also of the younger ages, are those involving $[Ba/Al]$, which has some of the highest correlation coefficients in the three galactocentric regions. As can be seen in Table A.3, the adjusted coefficients of determination using the $[Ba/Al]$ ratio are 0.75, 0.57, and 0.84 for the outer, solar, and inner regions, respectively. On the other hand, the global relation has a lower correlation coefficient of 0.55.

As shown in Table 2, the accuracy obtained with the $[Ba/Al]$ relation is 0.1 Gyr in the outer region, -1.4 Gyr in the solar region, and -0.0 Gyr in the inner region, with precisions of 0.9, 2.4, and 0.4 Gyr, respectively. However, if we exclude in the solar region, the three most discrepant clusters, NGC6791, Berkeley 44, and Collinder 261, which are likely subject to migration

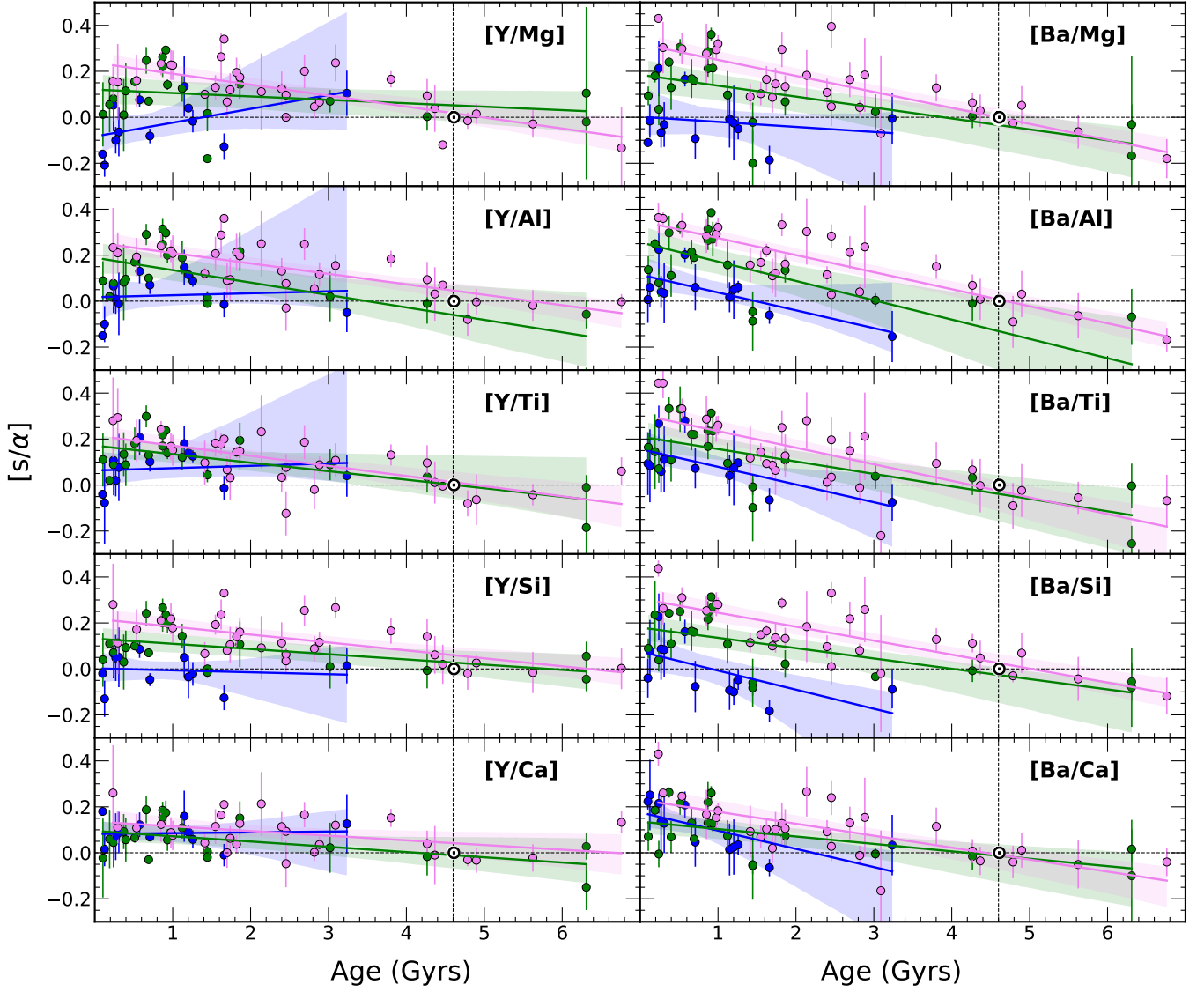


Fig. 5: Age versus $[s/\alpha]$ for our OC sample divided among the three R_{GC} regions. The regression curves with their confidence intervals (shaded regions) are shown in each panel. On the left side, we have the abundance ratios $[Y/\alpha]$ versus age, and on the right side we have $[Ba/\alpha]$ versus age. The symbols and colours are the same as in Fig. 3.

(see Section 4.3), the accuracy improves, decreasing to ~ -0.9 Gyr, and the precision becomes slightly lower at 2.3 Gyr. These numbers give us a first estimate of the kind of uncertainties to which ages measured with chemical clocks are subject.

5.2. Ages of individual member stars

Another interesting test is to compare the age of each cluster member with the age obtained from one of our best relations. We selected the ages computed with the relations based on the abundance ratio $[Ba/Al]$ as an example. This comparison allowed us to make a more realistic estimate of the uncertainties when the relation is applied to the field stars. Within the same cluster, there can be considerable variations in abundance ratios, which are linked to the quality of the measurements and some peculiar enrichment in Ba and in other s -process elements. This results in variations between the estimated ages of members of the same clusters, which are expected to be coeval. In Figure 9, we show

the violin plots of the ages of each stellar member of the clusters calculated using the relations between $[Ba/Al]$ and age, derived independently in the three radial regions. We compare the individual ages with the literature ages from Cantat-Gaudin et al. (2020). In the outer and inner discs, the isochrone fitting ages for almost all clusters falls within the interquartile range of the ages calculated with our relations. However, in the solar region, this does not happen for some clusters, such as NGC6791, Collinder 261, NGC4815, or Berkeley 44. As discussed in Section 4.3, this supports the high probability of these clusters being subject to migration. We suppose that they were born in the inner disc, as evidenced by their R_g . We then did a further test, calculating their ages with the relation obtained for the inner disc. We have an improvement for NGC6791 and Berkeley 44, while the age of Collinder 261 remains discrepant. We also have to consider that the age given for NGC6791 by Cantat-Gaudin et al. (2020) is a lower limit, and there are many works that give higher ages for this cluster (e.g. Brogaard et al. 2011, 2012, 2021); thus, they are

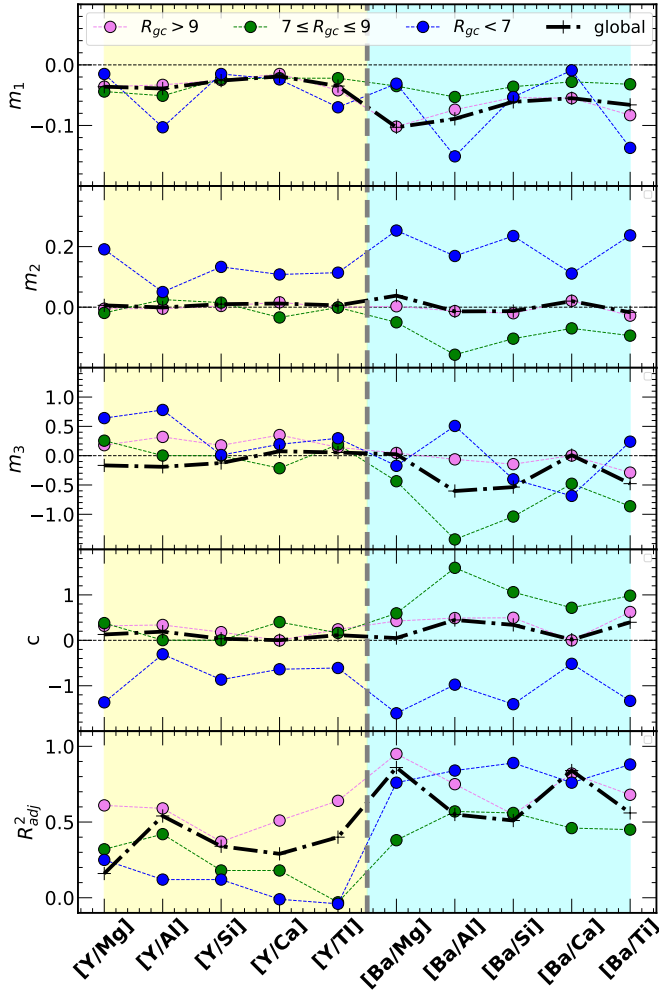


Fig. 6: Regression coefficients for the $[s-\alpha] = m_1 \cdot \text{age} + m_2 \cdot R_{GC} + m_3 \cdot [\text{Fe}/\text{H}] + c$ relation. We show m_1 in the upper panel, m_2 in the second one, m_3 in the third one, and c in the fourth one. In the bottom panel, we present the correlation coefficients. In all panels, we use the following symbols: blue circles for the inner region, green circles for the solar region, pink circles for the outer region, and dashed black lines for the whole sample. The yellow region highlights the abundance ratios with Y, and the cyan region shows them with Ba.

similar to the age obtained with our relations. Furthermore, the above seems to be supported by the fact that other clusters in the solar region that appear to deviate in Figure 9 (e.g. NGC6709, Pismis15, NGC5822, NGC6633, NGC2516) have R_{GC} at the edge with the inner region (between 7-7.5 kpc).

6. Application to field stars

The last step of our analysis was to verify the applicability of the relations to the field stars. To do this, we needed to select a sample of field stars with similar characteristics to those of the clusters with which we calibrated the relations. They must therefore be thin-disc stars, in approximately the same $[\text{Fe}/\text{H}]$ range as our open cluster sample, and their ages must not exceed 7 Gyr. The age constraint is the most difficult to obtain, because we know that the determination of the age of field stars with isochrone fitting is extremely uncertain. We thus relaxed this constraint,

Table 2: Accuracy and precision of our relations in recovering the ages of clusters in each of the defined regions and globally.

$R_{GC} > 9$		
ratio	accuracy (Gyr)	precision (Gyr)
[Y II/Mg I]	-0.2	2.1
[Y II/Al I]	0.6	2.2
[Y II/Si I]	0.1	2.9
[Y II/Ca I]	-0.1	4.7
[Y II/Ti I]	0.2	1.7
[Ba II/Mg I]	-0.5	1.0
[Ba II/Al I]	0.1	0.9
[Ba II/Si I]	0.3	1.3
[Ba II/Ca I]	-0.5	2.0
[Ba II/Ti I]	0.1	1.1
$7 < R_{GC} < 9$ (kpc)*		
[Y II/Mg I]	-1.6 (-1.6)	2.8 (2.1)
[Y II/Al I]	-0.3 (-0.1)	2.1 (1.9)
[Y II/Si I]	0.5 (0.6)	3.4 (3.5)
[Y II/Ca I]	-1.3 (-0.9)	3.3 (3.3)
[Y II/Ti I]	-0.7 (-0.1)	3.8 (3.1)
[Ba II/Mg I]	-0.3 (0.3)	3 (2.4)
[Ba II/Al I]	-1.4 (-0.9)	2.4 (2.3)
[Ba II/Si I]	-0.4 (-0.3)	2.9 (2.6)
[Ba II/Ca I]	-0.3 (-0.1)	2.6 (2.6)
[Ba II/Ti I]	-0.6 (0.1)	2.8 (2.5)
$R_{GC} < 7$ (kpc)		
[Y II/Mg I]	2.0	7.0
[Y II/Al I]	-0.1	0.8
[Y II/Si I]	1.2	4.9
[Y II/Ca I]	0.9	2.9
[Y II/Ti I]	-0.4	1.3
[Ba II/Mg I]	0.7	2.3
[Ba II/Al I]	-0.0	0.4
[Ba II/Si I]	0.2	0.9
[Ba II/Ca I]	2.2	5.5
[Ba II/Ti I]	-0.1	0.4
$6 < R_{GC} < 20$ (kpc)		
[Y II/Mg I]	-1.3	3.1
[Y II/Al I]	-0.3	2.7
[Y II/Si I]	0.0	3.2
[Y II/Ca I]	-0.3	3.7
[Y II/Ti I]	-0.1	2.4
[Ba II/Mg I]	-1.2	1.5
[Ba II/Al I]	-0.6	1.3
[Ba II/Si I]	-0.3	1.7
[Ba II/Ca I]	-0.2	1.8
[Ba II/Ti I]	-0.2	1.5

* Results after removing discrepant OCs are included in parentheses.

but we have to take it into account when we measure very old ages for stars with our relations. Those ages fall outside the limits for which they were calibrated. We used a chemical criterion to discriminate stars potentially outside the thin disc, based on the separation proposed by Adibekyan et al. (2012), obtaining a sample of about 2600 thin disc stars.

As in the previous test, we show an illustrative case here, presenting the results from the relationship with the best correlation, accuracy, and precision, that is the one between age and $[\text{Ba}/\text{Al}]$.

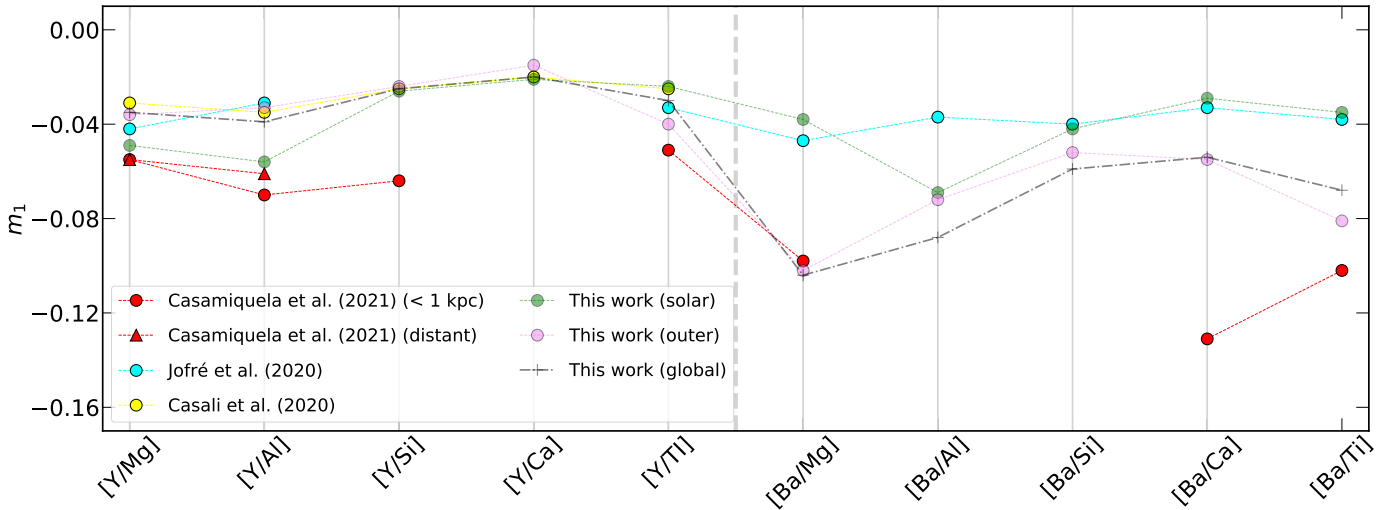


Fig. 7: Comparison of first independent variable ($m_1 \cdot \text{age}$) of our stellar dating relations with those of Casali et al. (2020) (yellow) for solar-like stars (which were tested in open clusters), Jofré et al. (2020) for a sample of 80 solar twins (cyan), and those of Casamiquela et al. (2021) for a sample of 47 open clusters (red).

In Fig. 10, we show $[\alpha/\text{Fe}]^1$ versus $[\text{Fe}/\text{H}]$, separating the three radial regions. Our sample is dominated by the solar neighbourhood stars by construction (Stonkutė et al. 2016), and the inner and outer bins are under-sampled. The results of the age distribution in $[\alpha/\text{Fe}]$ - $[\text{Fe}/\text{H}]$ plane agree with the expectation for the age distribution in the thin disc (see, e.g. Haywood et al. 2013; Hayden et al. 2015; Buder et al. 2019; Casali et al. 2019, 2020). The oldest stars are those with a higher $[\alpha/\text{Fe}]$ ratio, while the youngest have solar or slightly sub-solar ratios. There are few α -enhanced stars at high metallicity and of intermediate age. We remind the reader that these are only probabilistic indications of age and not real measurements. For field stars, the scatter in abundance ratios of age tracers at a given age (calculated with isochrones) is about 0.2 dex. This makes the age determination with chemical clocks only approximate and of purely statistical value.

7. Summary and conclusions

Here, we list some considerations and caveats on the limit of the relations providing ages based on chemical clocks (related to chemical evolution), such as the ones used in the present work.

- i. **The role of star formation history (SFH)** –Such relations can only be applied to the same populations from which they were derived. Since the abundance ratios $[s/\alpha]$ strongly depend on the SFH, we recommend only using the relations calibrated with open clusters for the thin disc field population, in the same metallicity interval sampled by the calibrators used. Ages older than those of the calibrators are a dangerous extrapolation.
- ii. **The role of migration** –Field stars can migrate. Although we saw that the effect on the slopes of our relations due to blurring on open clusters is limited, this effect might be larger for field stars, and it can be combined with an even stronger effect of churning. There are some empirical methods based on deriving, for each star, its birth radius using its current metallicity, R_{GC} , and an observed or modelled radial metallicity

gradient (see, e.g. Feltzing et al. 2017; Quillen et al. 2018). These methods introduce other uncertainties depending on the choice of gradient and its time evolution, particularly for older stars. So, we point out that the ages derived with the relations of the present work do not take into account migration, and if the effect of migration is greater than the size of the radial bin under consideration, they may provide incorrect ages. This is especially true in the inner disc, where migration to the outer disc dominates, but it can also affect the outer disc since stellar migration can be bi-directional.

- iii. **The non-uniqueness of the results** –In this paper, we provide ten different relationships: five based on Y and five based on Ba. Although the relationships are in general agreement, they do not provide the same age for each star. We preferred to leave the relationships separate so that, depending on which abundances are available, it might be possible to provide an age estimate. The simultaneous use of several indicators gives an idea of the range of possible ages. We remind the reader that our relations are not to be used for an individual measurement of the age of field stars, but to statistically infer the age distribution of a population or characterise a single star as young, intermediate-age, or old.

At the moment, this is the best we can do. With our sample of clusters, we mapped the spatial variations of the age-chemical-clock relationships. We confirm that these are not unique and that they vary more in the inner disc. Although the cluster sample is the largest used so far, it has an inherent limitation due to the characteristic of cluster populations: it is a thin-disc population with young and intermediate ages. In particular, the inner disc population being subject to more destructive effects is limited to clusters younger than 3 Gyr. This is a general limit that is not related to our sample but is also visible in larger samples (Cantat-Gaudin et al. 2020). The strong recommendation we repeat is not to extrapolate the relationships into unmapped intervals from the clusters, and not to apply it to populations other than the thin disc. In the future, samples combining asteroseismological and spectroscopic observations will help us to extend the relationships to older ages and to populations other than the thin disc.

¹ $[\alpha/\text{Fe}]$ is computed as $([\text{Mg}/\text{Fe}] + [\text{Si}/\text{Fe}] + [\text{Ca}/\text{Fe}] + [\text{Ti}/\text{Fe}])/4$

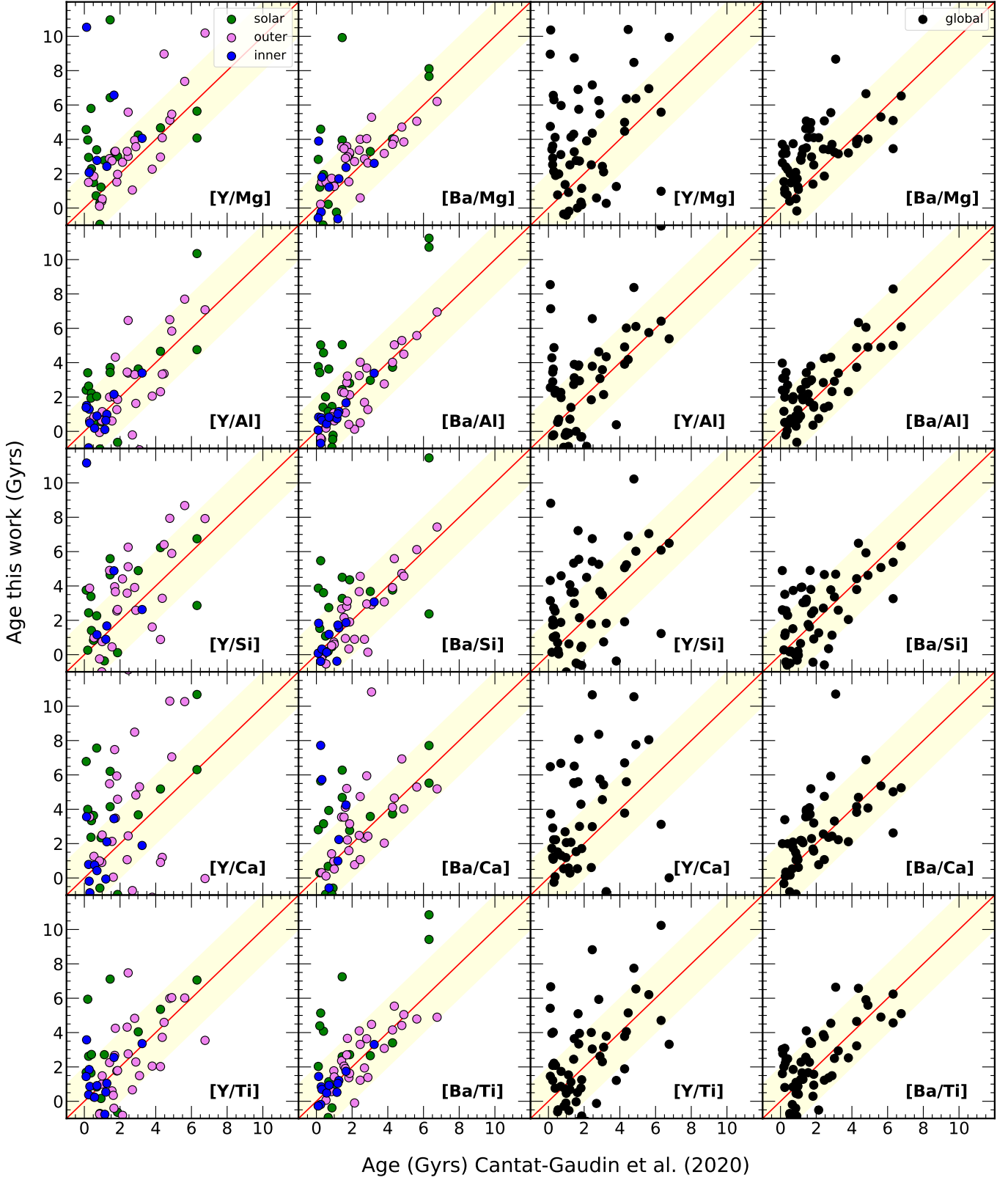


Fig. 8: Ages computed with our relations versus ages from isochrone fitting (Cantat-Gaudin et al. 2020). In the left panels, we show the ages computed with the relations obtained for each radial region. The clusters are colour-coded by R_{GC} . In the two right panels, we show the ages computed with global relations versus the ages from Cantat-Gaudin et al. (2020). The red continuous line is the bisector and indicates the 1-to-1 relation. The yellow shaded regions indicate the clusters with ages within 2 Gyr from their age from the isochrone fitting.

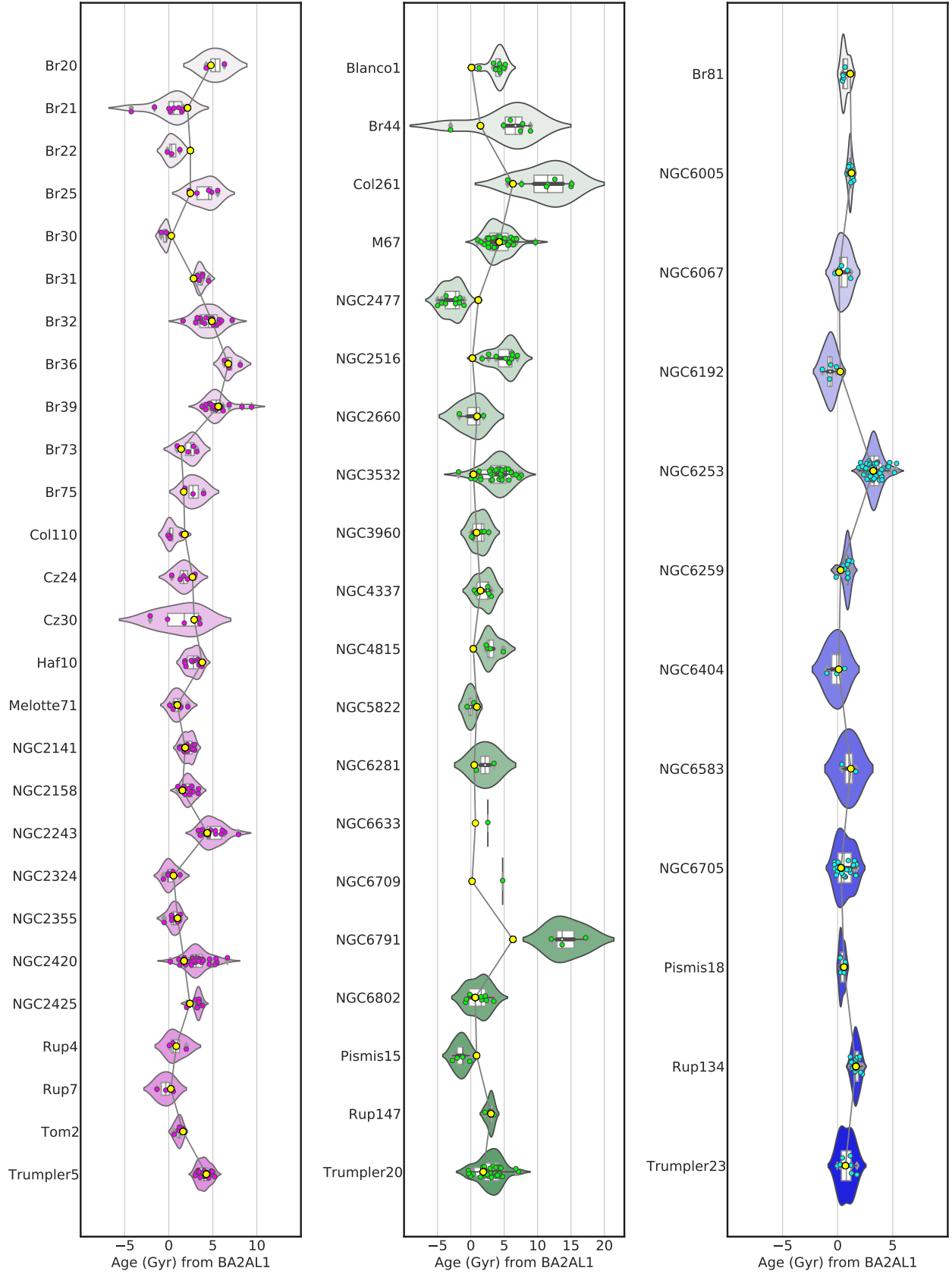


Fig. 9: Violin plots of the ages of each stellar member of the clusters calculated using the relations inferred from $[Ba/Al]$ for each of the three regions. Each of the coloured dots represents the age of each member star calculated individually, while the yellow dot is the age from Cantat-Gaudin et al. (2020) for each of the clusters. The thick white bar in the center represents the interquartile range and the thin grey line represents the $1.5 \times IQR$, also showing a kernel density estimation with the distribution shape of the data. The left panel shows the clusters in the outer disc, the central panel those in the solar region, and the right one the inner disc clusters.

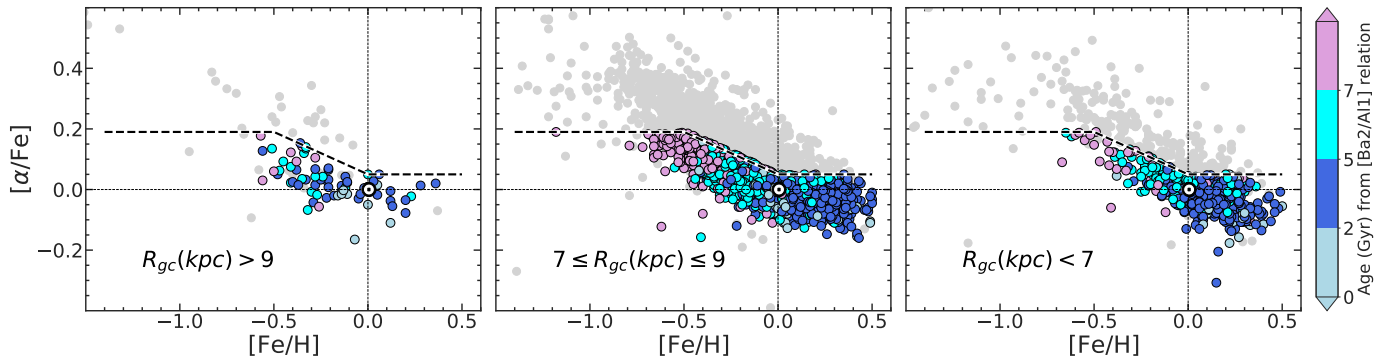


Fig. 10: $[\text{Fe}/\text{H}]$ versus $[\alpha/\text{Fe}]$ for field stars in the three radial regions coloured with the inferred ages using the $[\text{Ba}/\text{Al}]$ relations computed for each radial region. The dashed black line is the dividing line given by Adibekyan et al. (2012). In the background (grey), we show the field stars excluded from our selection, which are presumably thick-disc and halo stars.

In the present work, we provided a set of multiple weighted linear regressions in three variables ($[\text{Fe}/\text{H}]$, R_{GC} , and age) between abundance ratios, the so-called chemical clocks, and stellar ages, which were calibrated with an appropriate sample of open clusters, the ages and distances of which were homogeneously determined using *Gaia* DR2. We estimate the accuracy and precision of each relation in recovering the age of open clusters. Among the considered chemical clocks, $[\text{Ba}/\text{Al}]$, and in general abundance ratios involving barium, provide the best recovering factor. The relation between $[\text{Ba}/\text{Al}]$ and age is also able to reproduce the ages of the individual member stars with a precision better than 2 Gyr. Considering that typical errors on the ages of giant stars by isochrone fitting can reach 100%, the result is very encouraging. In the solar region, this relationship does not work for some clusters (e.g. NGC6791, Berkeley 44, NGC4815, and Collinder 261), which are likely subjects of migration. We applied our relations to a sample of thin-disc field stars, selected from the *Gaia*-ESO DR6 catalogue. This ensures that we have a homogeneous analysis with respect to the clusters used to calibrate the relationships. Since the sample of field stars contains both dwarfs and giants, we used a solar scale based on giants and dwarfs of M67 to avoid any offset between the two samples. Using chemical information, we separated the field sample in Galactic populations: thin disc, thick disc, and halo. We only considered thin-disc stars in each radial region, in approximately the same $[\text{Fe}/\text{H}]$ range of the open clusters used to calibrate the relations. We computed their ages: the distribution of ages in the $[\alpha/\text{Fe}]$ versus $[\text{Fe}/\text{H}]$ plane show the expected behaviour with youngest stars at high $[\text{Fe}/\text{H}]$ and low $[\alpha/\text{Fe}]$, and the oldest ones at low $[\text{Fe}/\text{H}]$ and high $[\alpha/\text{Fe}]$. Finally, we discuss the limits of our method and give some important recommendations on the use of ages from chemical clocks based on chemical evolution. We state that future improvements can be made through the use of large asteroseismic samples combined with high-resolution spectroscopy, which will allow us to obtain calibrators in the old age regime, which are currently missing. In a forthcoming paper, we aim also to discuss the origin of the radial variations of the $[s/\alpha]$ ratios in detail and in terms of chemical evolution and stellar nucleosynthesis.

Acknowledgements. We thank an anonymous referee for her/his careful reading and valuable comments to the first version of the manuscript. Based on data products from observations made with ESO Telescopes at the La Silla Paranal Observatory under programme ID 188.B-3002. These data products have been processed by the Cambridge Astronomy Survey Unit (CASU) at the Institute of Astronomy, University of Cambridge, and by the FLAMES/UVES reduction team at INAF/Osservatorio Astrofisico di Arcetri. These data have been obtained from the *Gaia*-ESO Survey Data Archive, prepared and hosted by the Wide Field As-

tronomy Unit, Institute for Astronomy, University of Edinburgh, which is funded by the UK Science and Technology Facilities Council. This work was partly supported by the European Union FP7 programme through ERC grant number 320360 and by the Leverhulme Trust through grant RPG-2012-541. We acknowledge the support from INAF and Ministero dell' Istruzione, dell' Università e della Ricerca (MIUR) in the form of the grant "Premiale VLT 2012" and "Premiale 2016 MITIC". The results presented here benefit from discussions held during the *Gaia*-ESO workshops and conferences supported by the ESF (European Science Foundation) through the GREAT Research Network Programme. This work has made use of data from the European Space Agency (ESA) mission *Gaia* (<https://www.cosmos.esa.int/gaia>), processed by the *Gaia* Data Processing and Analysis Consortium (DPAC, <https://www.cosmos.esa.int/web/gaia/dpac/consortium>). Funding for the DPAC has been provided by national institutions, in particular the institutions participating in the *Gaia* Multilateral Agreement. CVV and LM thank the COST Action CA18104: MW-Gaia. TB was funded by grant No. 2018-04857 from The Swedish Research Council. F.J.E. acknowledges financial support by the spanish grant PGC2018-101950-B-I00 and MDM-2017-0737 at Centro de Astrobiología (CSIC-INTA), Unidad de Excelencia María de Maeztu, and from the European Union's Horizon 2020 research and innovation programme under Grant Agreement no. 824064 through the ESCAPE - The European Science Cluster of Astronomy & Particle Physics ESFRI Research Infrastructures project. CVV is especially grateful to Andrés Moya Bedón (University of Valencia) for his support and help.

References

- Adibekyan, V. Z., Sousa, S. G., Santos, N. C., et al. 2012, *A&A*, 545, A32
- Anders, F., Chiappini, C., Minchev, I., et al. 2017, *A&A*, 600, A70
- Arlandini, C., Käppeler, F., Wisshak, K., et al. 1999, *ApJ*, 525, 886
- Baratella, M., D'Orazi, V., Carraro, G., et al. 2020, *A&A*, 634, A34
- Baratella, M., D'Orazi, V., Sheminova, V., et al. 2021, *A&A*, 653, A67
- Battistini, C. & Bensby, T. 2016, *A&A*, 586, A49
- Bertelli Motta, C., Pasquali, A., Richer, J., et al. 2018, *MNRAS*, 478, 425
- Bertelli Motta, C., Salaris, M., Pasquali, A., & Grebel, E. K. 2017, *MNRAS*, 466, 2161
- Bertolli, M. G., Herwig, F., Pignatari, M., & Kawano, T. 2013, arXiv e-prints, arXiv:1310.4578
- Binney, J. & Tremaine, S. 2008, *Galactic Dynamics: Second Edition*
- Bisterzo, S., Travaglio, C., Gallino, R., Wiescher, M., & Käppeler, F. 2014, *ApJ*, 787, 10
- Bovy, J. 2015, *ApJS*, 216, 29
- Brogaard, K., Bruntt, H., Grundahl, F., et al. 2011, *A&A*, 525, A2
- Brogaard, K., Grundahl, F., Sandquist, E. L., et al. 2021, *A&A*, 649, A178
- Brogaard, K., VandenBerg, D. A., Bruntt, H., et al. 2012, *A&A*, 543, A106
- Buder, S., Lind, K., Ness, M. K., et al. 2019, *A&A*, 624, A19
- Busso, M., Vescovi, D., Palmerini, S., Cristallo, S., & Antonuccio-Delogu, V. 2021, *ApJ*, 908, 55
- Cantat-Gaudin, T., Anders, F., Castro-Ginard, A., et al. 2020, *A&A*, 640, A1
- Casali, G., Magrini, L., Tognelli, E., et al. 2019, *A&A*, 629, A62
- Casali, G., Spina, L., Magrini, L., et al. 2020, *A&A*, 639, A127
- Casamiquela, L., Soubiran, C., Jofré, P., et al. 2021, *A&A*, 652, A25
- Chen, Y. Q. & Zhao, G. 2020, *MNRAS*, 495, 2673
- Cowan, J. J. & Rose, W. K. 1977, *ApJ*, 212, 149
- De Silva, G. M., Freeman, K. C., Bland-Hawthorn, J., et al. 2015, *MNRAS*, 449, 2604

- Delgado Mena, E., Moya, A., Adibekyan, V., et al. 2019, A&A, 624, A78
- Delgado Mena, E., Tsantaki, M., Adibekyan, V. Z., et al. 2017, A&A, 606, A94
- D’Orazi, V., Magrini, L., Randich, S., et al. 2009, ApJ, 693, L31
- Feltzing, S., Howes, L. M., McMillan, P. J., & Stokutė, E. 2017, MNRAS, 465, L109
- Fuhrmann, K., Chini, R., Kaderhandt, L., Chen, Z., & Lachaume, R. 2017, MNRAS, 471, 3768
- Gaia Collaboration, Brown, A. G. A., Vallenari, A., et al. 2018, A&A, 616, A1
- Gaia Collaboration, Brown, A. G. A., Vallenari, A., et al. 2021, A&A, 649, A1
- Gaia Collaboration, Prusti, T., de Bruijne, J. H. J., et al. 2016, A&A, 595, A1
- Gilmore, G., Randich, S., Asplund, M., et al. 2012, The Messenger, 147, 25
- Grevesse, N., Asplund, M., & Sauval, A. J. 2007, Space Sci. Rev., 130, 105
- Halle, A., Di Matteo, P., Haywood, M., & Combes, F. 2015, A&A, 578, A58
- Hayden, M. R., Bovy, J., Holtzman, J. A., et al. 2015, ApJ, 808, 132
- Haywood, M., Di Matteo, P., Lehnert, M. D., Katz, D., & Gómez, A. 2013, A&A, 560, A109
- Howes, L. M., Lindegren, L., Feltzing, S., Church, R. P., & Bensby, T. 2019, A&A, 622, A27
- Jackson, R. J., Jeffries, R. D., Wright, N. J., et al. 2022, MNRAS, 509, 1664
- Jacobson, H. R. & Friel, E. D. 2013, AJ, 145, 107
- Jilková, L., Carraro, G., Jungwiert, B., & Minchev, I. 2012, A&A, 541, A64
- Jofré, P., Jackson, H., & Tucci Maia, M. 2020, A&A, 633, L9
- Liu, F., Asplund, M., Yong, D., et al. 2016, MNRAS, 463, 696
- Magrini, L., Lagarde, N., Charbonnel, C., et al. 2021a, A&A, 651, A84
- Magrini, L., Spina, L., Randich, S., et al. 2018, A&A, 617, A106
- Magrini, L., Vescovi, D., Casali, G., et al. 2021b, A&A, 646, L2
- Maiorca, E., Magrini, L., Busso, M., et al. 2012, ApJ, 747, 53
- Maiorca, E., Randich, S., Busso, M., Magrini, L., & Palmerini, S. 2011, ApJ, 736, 120
- Majewski, S. R., Schiavon, R. P., Frinchaboy, P. M., et al. 2017, AJ, 154, 94
- Marsakow, V. A., Gozha, M. L., Koval’, V. V., & Shpigel’, L. V. 2016, Astronomy Reports, 60, 61
- Messa, M., Adamo, A., Calzetti, D., et al. 2018, MNRAS, 477, 1683
- Mishenina, T., Korotin, S., Carraro, G., Kovtyukh, V. V., & Yegorova, I. A. 2013a, MNRAS, 433, 1436
- Mishenina, T., Pignatari, M., Carraro, G., et al. 2015, MNRAS, 446, 3651
- Mishenina, T. V., Pignatari, M., Korotin, S. A., et al. 2013b, A&A, 552, A128
- Netopil, M., Oralhan, I. A., Çakmak, H., Michel, R., & Karataş, Y. 2021, MNRAS, 500, 1000
- Nissen, P. E. 2016, A&A, 593, A65
- Nissen, P. E., Christensen-Dalsgaard, J., Mosumgaard, J. R., et al. 2020, A&A, 640, A81
- Önehag, A., Korn, A., Gustafsson, B., Stempels, E., & Vandenberg, D. A. 2011, A&A, 528, A85
- Pancino, E., Lardo, C., Altavilla, G., et al. 2017, A&A, 598, A5
- Quillen, A. C., Nolting, E., Minchev, I., De Silva, G., & Chiappini, C. 2018, MNRAS, 475, 4450
- Randich, S., Gilmore, G., & Gaia-ESO Consortium. 2013, The Messenger, 154, 47
- Randich, S., Gilmore, G. G., & Magrini, L. 2022, A&A, (submitted)
- Randich, S. & Magrini, L. 2021, Frontiers in Astronomy and Space Sciences, 8, 6
- Reddy, A. B. S. & Lambert, D. L. 2017, ApJ, 845, 151
- Sacco, G. G., Morbidelli, L., Franciosini, E., et al. 2014, A&A, 565, A113
- Sales-Silva, J. V., Daflon, S., Cunha, K., et al. 2021, arXiv e-prints, arXiv:2112.02196
- Schönrich, R. & Binney, J. 2009, MNRAS, 396, 203
- Sellwood, J. A. & Binney, J. J. 2002, MNRAS, 336, 785
- Skúladóttir, Á., Hansen, C. J., Salvadori, S., & Choplin, A. 2019, A&A, 631, A171
- Slumstrup, D., Grundahl, F., Brogaard, K., et al. 2017, A&A, 604, L8
- Smiljanic, R., Korn, A. J., Bergemann, M., et al. 2014, A&A, 570, A122
- Soderblom, D. R., Hillenbrand, L. A., Jeffries, R. D., Mamajek, E. E., & Naylor, T. 2014, Protostars and Planets VI, 219
- Souto, D., Allende Prieto, C., Cunha, K., et al. 2019, ApJ, 874, 97
- Spina, L., Meléndez, J., Karakas, A. I., et al. 2018, MNRAS, 474, 2580
- Spina, L., Meléndez, J., Karakas, A. I., et al. 2016, A&A, 593, A125
- Spina, L., Nordlander, T., Casey, A. R., et al. 2020, ApJ, 895, 52
- Stokutė, E., Koposov, S. E., Howes, L. M., et al. 2016, MNRAS, 460, 1131
- Tautvaišienė, G., Viscasillas Vázquez, C., Mikolaitis, Š., et al. 2021, A&A, 649, A126
- Titarenko, A., Recio-Blanco, A., de Laverny, P., Hayden, M., & Guiglion, G. 2019, A&A, 622, A59
- Trippella, O., Busso, M., Palmerini, S., Maiorca, E., & Nucci, M. C. 2016, ApJ, 818, 125
- Tucci Maia, M., Ramírez, I., Meléndez, J., et al. 2016a, A&A, 590, A32
- Tucci Maia, M., Ramírez, I., Meléndez, J., et al. 2016b, A&A, 590, A32
- Yong, D., Carney, B. W., & Friel, E. D. 2012, AJ, 144, 95
- Zhang, H., Chen, Y., & Zhao, G. 2021, ApJ, 919, 52
- Zinn, J. C., Stello, D., Elsworth, Y., et al. 2021, arXiv e-prints, arXiv:2108.05455
-
- ¹ Institute of Theoretical Physics and Astronomy, Vilnius University, Sauletekio av. 3, 10257 Vilnius, Lithuania e-mail: carlos.viscasillas@ff.vu.lt
- ² INAF - Osservatorio Astrofisico di Arcetri, Largo E. Fermi 5, 50125, Firenze, Italy e-mail: laura.magrini@inaf.it
- ³ Dipartimento di Fisica e Astronomia, Università degli Studi di Bologna, Via Gobetti 93/2, I-40129 Bologna, Italy
- ⁴ INAF - Osservatorio di Astrofisica e Scienza dello Spazio di Bologna, via Gobetti 93/3, 40129, Bologna, Italy
- ⁵ INAF - Padova Observatory, Vicolo dell’Osservatorio 5, 35122 Padova, Italy
- ⁶ Lund Observatory - Department of Astronomy and Theoretical Physics, Box 43, SE-22100 Lund, Sweden
- ⁷ Department of Astronomy - Indiana University, Swain West 318 727 East Third Street, Bloomington, IN 47405, USA
- ⁸ Departamento de Astrofísica, Centro de Astrobiología (CSIC-INTA), ESAC Campus, Camino Bajo del Castillo s/n, E-28692 Villanueva de la Cañada, Madrid, Spain
- ⁹ Instituto de Astrofísica e Ciências do Espaço, Universidade do Porto, CAUP, Rua das Estrelas, 4150-762 Porto, Portugal
- ¹⁰ Departamento de Física de la Tierra y Astrofísica and IPARCOS UCM, Universidad Complutense de Madrid, E-28040, Madrid, Spain
- ¹¹ Leibniz-Institut für Astrophysik Potsdam, An der Sternwarte 16, 14482 Potsdam, Germany
- ¹² Centro de Astrobiología (CSIC-INTA), Carretera de Ajalvir km 4, Torrejón de Ardoz, 28850, Madrid, Spain
- ¹³ Institute of Astronomy, University of Cambridge, Madingley Road, Cambridge CB3 0HA, United Kingdom
- ¹⁴ Instituto de Astrofísica de Andalucía, CSIC, Glorieta de la Astronomía, E-18080, Granada, Spain
- ¹⁵ GEPI, Observatoire de Paris, CNRS, Université Paris Diderot, 5 Place Jules Janssen, 92190 Meudon, France
- ¹⁶ Observational Astrophysics, Department of Physics and Astronomy, Uppsala University, Box 516, 75120 Uppsala, Sweden
- ¹⁷ Nicolaus Copernicus Astronomical Center, Polish Academy of Sciences, ul. Bartycka 18, 00-716, Warsaw, Poland
- ¹⁸ Max-Planck Institut für Astronomie, Königstuhl 17, 69117 Heidelberg, Germany

Appendix A: Additional material

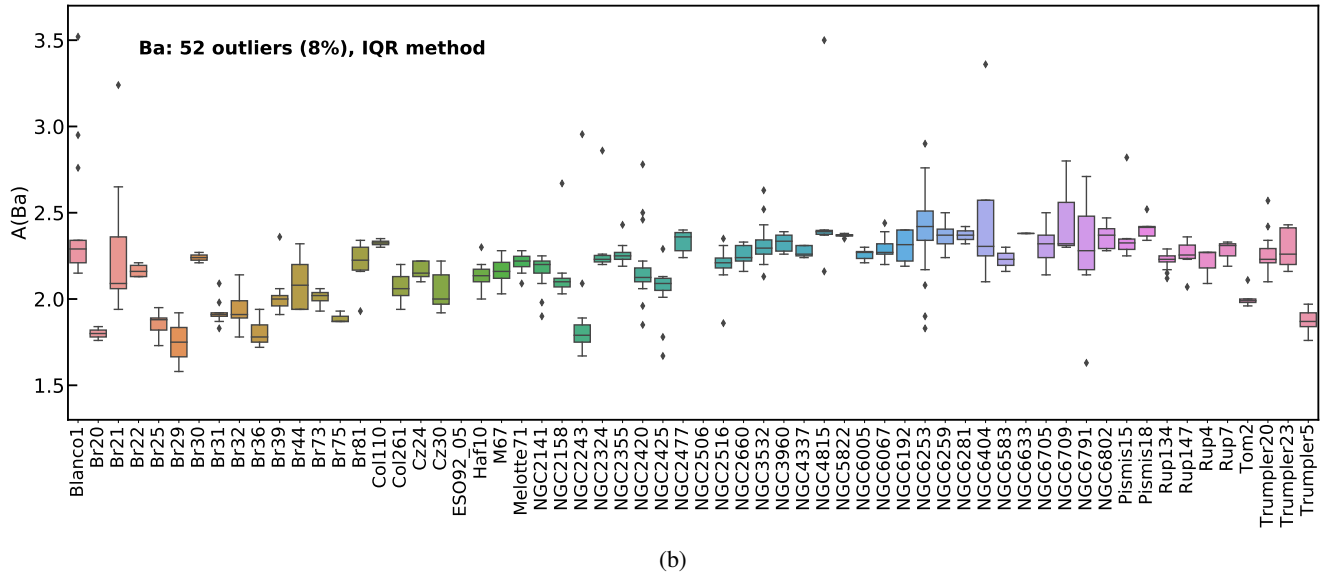
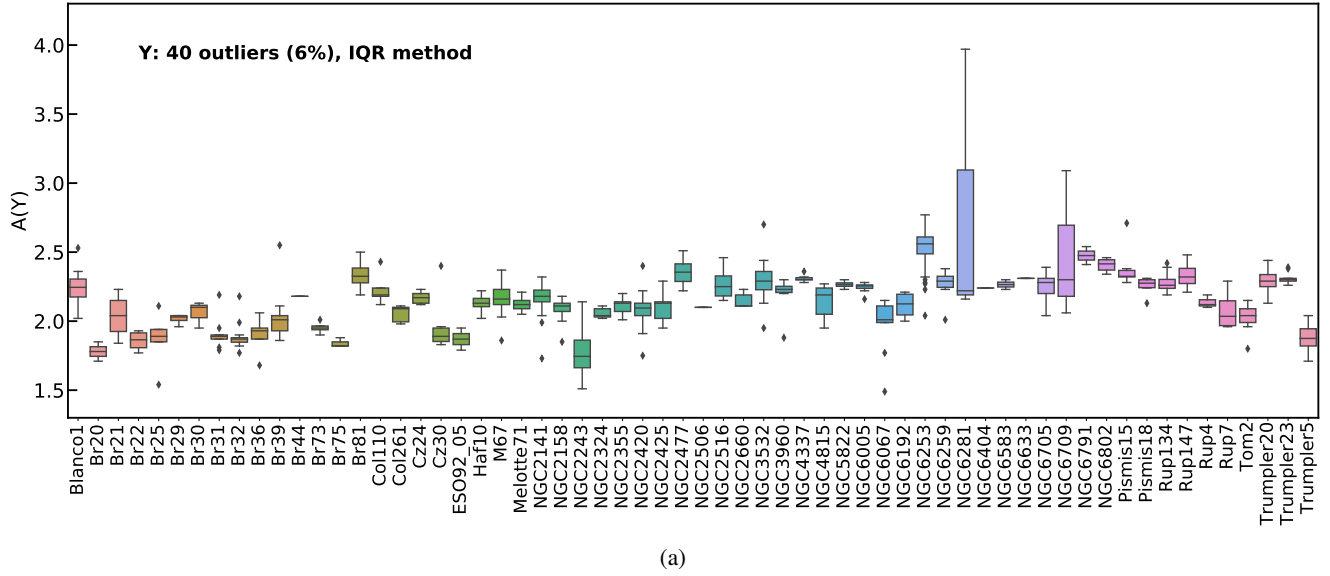


Fig. A.1: Box plots with the interquartile range of the abundance for each of the clusters with the outliers (observations that fall below $Q1 - 1.5 \text{ IQR}$ or above $Q3 + 1.5 \text{ IQR}$). Figure A.1a for Y2 and A.1b for Ba2.

Table A.1.: Average [s-/H] and [s-/Fe] for our sample of open clusters

GES_FLD	[Fe/H]	Age (Gyr)	R _{GC} (kpc)	[Y/H]	[Zr/H]	[Ba/H]	[La/H]	[Ce/H]	[Y/H]	[Zr/Fe]	[Ba/Fe]	[La/Fe]	[Ce/Fe]
Blanco 1	-0.03	0.1	8.3	0.0	-0.04	0.05	0.12	-0.06	0.02	0.02	0.09	0.13	-0.02
Berkeley 20	-0.38	4.79	16.32	-0.31	-0.34	-0.32	-0.33	-0.34	0.06	0.03	0.06	0.1	0.04
Berkeley 21	-0.21	2.14	14.73	-0.05	-0.21	0.06		-0.04	0.16	0.01	0.29		0.19
Berkeley 22	-0.26	2.45	14.29	-0.23	-0.32	0.04		-0.27	0.04	-0.02	0.28		0.11
Berkeley 25	-0.25	2.45	13.81	-0.2	-0.25	-0.27	-0.27	-0.3	0.11	0.05	0.07	0.09	0.03
Berkeley 29	-0.36	3.09	20.58	-0.08	-0.08	-0.37			0.32		-0.0		
Berkeley 30	-0.13	0.3	13.25	-0.03	-0.08	0.12	0.13	0.06	0.12	0.09	0.27	0.28	0.21
Berkeley 31	-0.31	2.82	15.09	-0.2	-0.21	-0.22	-0.17	-0.13	0.13	0.05	0.1	0.18	0.2
Berkeley 32	-0.29	4.9	11.14	-0.23	-0.18	-0.18	-0.15	-0.21	0.06	0.1	0.1	0.13	0.07
Berkeley 36	-0.15	6.76	11.73	-0.14	-0.11	-0.31	0.07	-0.14	0.01	0.12	-0.08	0.33	0.01
Berkeley 39	-0.14	5.62	11.49	-0.12	-0.07	-0.14	-0.05	-0.07	0.02	0.07	-0.0	0.09	0.06
Berkeley 44	0.22	1.45	7.01	0.09	0.14	-0.01		0.1	-0.03	-0.04	-0.22		-0.12
Berkeley 73	-0.26	1.41	13.76	-0.16	-0.19	-0.11	-0.12	-0.09	0.11	0.08	0.14	0.12	0.17
Berkeley 75	-0.34	1.7	14.67	-0.25	-0.37	-0.23	-0.25	-0.26	0.1	0.02	0.12	0.14	0.12
Berkeley 81	0.22	1.15	5.88	0.24	0.22	0.13	0.3	0.3	0.02	0.01	-0.08	0.09	0.07
Collinder 110	-0.1	1.82	10.29	0.09	-0.02	0.2	0.11	0.14	0.17	0.07	0.31	0.17	0.23
Collinder 261	-0.05	6.31	7.26	-0.04	-0.03	-0.05	0.04	-0.08	0.01	0.02	0.0	0.07	-0.0
Czernik 24	-0.11	2.69	12.29	0.08	-0.01	0.04	0.16	0.07	0.19	0.09	0.15	0.26	0.18
Czernik 30	-0.31	2.88	13.78	-0.21	-0.2	-0.07		-0.08	0.11	0.14	0.26		0.24
ESO92_05	-0.29	4.47	12.82	-0.22	-0.23				0.11	0.1			
Haffner 10	-0.1	3.8	10.82	0.04	-0.03	0.0	0.05	0.03	0.15	0.08	0.11	0.17	0.14
M 67	0.0	4.27	8.96	0.0	0.0	0.0	0.02	-0.01	0.03	-0.01	0.02	0.03	-0.01
Melotte 71	-0.15	0.98	9.87	0.04	0.03	0.11	0.05	0.05	0.19	0.14	0.22	0.21	0.17
NGC 2141	-0.04	1.86	13.34	0.11	0.03	0.07	0.14	0.07	0.15	0.07	0.12	0.16	0.11
NGC 2158	-0.15	1.55	12.62	0.02	0.0	-0.02	0.04	0.01	0.18	0.17	0.15	0.19	0.18
NGC 2243	-0.45	4.37	10.58	-0.33	-0.39	-0.35	-0.38	-0.38	0.12	0.09	0.11	0.08	0.09
NGC 2324	-0.18	0.54	12.08	-0.03	-0.1	0.11	-0.11	-0.03	0.15	0.08	0.29	0.07	0.16
NGC 2355	-0.13	1.0	10.11	0.02	0.04	0.13	0.06	0.06	0.12	0.14	0.23	0.16	0.16
NGC 2420	-0.15	1.74	10.68	-0.05	0.01	-0.01	0.04	0.0	0.13	0.16	0.16	0.19	0.16
NGC 2425	-0.12	2.4	10.92	0.0	-0.05	-0.03	0.09	-0.01	0.08	0.06	0.1	0.19	0.12
NGC 2477	0.14	1.12	8.85	0.22	0.18	0.19	0.13	0.17	0.35	0.08	0.04	0.02	0.06
NGC 2506	-0.34	1.66	10.62	0.01									
NGC 2516	-0.04	0.24	8.32	0.05		0.02	-0.31		0.1		0.06		
NGC 2660	-0.05	0.93	8.98	0.06	0.01	0.13	0.12	0.14	0.11	0.06	0.18	0.17	0.19
NGC 3532	-0.03	0.4	8.19	0.09	0.09	0.11	0.07	0.2	0.1	0.09	0.12	0.09	0.19
NGC 3960	0.0	0.87	7.68	0.15	0.09	0.22	0.18	0.16	0.15	0.09	0.22	0.17	0.16
NGC 4337	0.24	1.45	7.45	0.21	0.19	0.15	0.15	0.18	-0.03	-0.06	-0.1	-0.11	-0.08
NGC 4815	0.08	0.37	7.07	0.05	0.08	0.27	0.02	0.18	0.06	0.1	0.25	0.06	0.17
NGC 5822	0.02	0.91	7.69	0.18	0.1	0.25	0.12	0.14	0.16	0.08	0.24	0.11	0.13
NGC 6005	0.22	1.26	6.51	0.16	0.21	0.14	0.06	0.16	-0.05	-0.01	-0.08	-0.16	-0.06
NGC 6067	0.03	0.13	6.78	-0.02	0.09	0.16	-0.02	0.02	-0.02	0.16	0.23	0.01	0.05
NGC 6192	-0.08	0.24	6.73	0.02	0.02	0.18	0.12	0.09	0.11	0.1	0.27	0.22	0.18
NGC 6253	0.34	3.24	6.88	0.36	0.21	0.25	0.31	0.25	0.02	-0.03	-0.09	-0.01	0.02
NGC 6259	0.18	0.27	6.18	0.2	0.16	0.25	0.17	0.28	0.03	-0.03	0.06	-0.01	0.1

Table A.1: continued.

GES_FLD	[Fe/H]	Age (Gyr)	R _{GC} (kpc)	[Y/H]	[Zr/H]	[Ba/H]	[La/H]	[Ce/H]	[Y/H]	[Zr/Fe]	[Ba/Fe]	[La/Fe]	[Ce/Fe]
NGC 6281	-0.04	0.51	7.81	0.1	0.04	0.25	0.14	0.14	0.14	0.09	0.3	0.15	0.18
NGC 6404	0.01	0.1	5.85	0.15	-0.14	0.12	0.08	0.13	0.2	-0.11	0.17	0.06	0.12
NGC 6583	0.22	1.2	6.32	0.18		0.11		0.23	-0.04		-0.11		0.02
NGC 6633	-0.03	0.69	8.0	0.1		0.19	0.03		0.09		0.18	0.02	
NGC 6705	0.03	0.31	6.46	0.15	0.08	0.19	0.14	0.18	0.11	0.05	0.15	0.11	0.15
NGC 6709	-0.02	0.19	7.6	0.03	0.01	0.16	0.1	0.07	0.08	0.08	0.2	0.17	0.14
NGC 6791	0.22	6.31	7.94	0.38		0.17	0.21	0.34	0.06		-0.02	-0.11	0.12
NGC 6802	0.14	0.66	7.14	0.32	0.2	0.24	0.13	0.22	0.19	0.06	0.11	-0.0	0.08
Pismis 15	0.02	0.87	8.62	0.24	0.1	0.19	0.24	0.18	0.2	0.08	0.15	0.19	0.14
Pismis 18	0.14	0.58	6.94	0.19	0.17	0.27	0.22	0.19	0.04	0.02	0.14	0.09	0.04
Ruprecht 134	0.27	1.66	6.09	0.17	0.21	0.11	0.12	0.2	-0.09	-0.06	-0.16	-0.15	-0.06
Ruprecht 147	0.12	3.02	8.05	0.12		0.1	0.06		0.0		-0.03	-0.06	
Ruprecht 4	-0.13	0.85	11.68	0.05	-0.09	0.09	0.11	0.11	0.18	0.06	0.22	0.25	0.24
Ruprecht 7	-0.24	0.23	13.11	-0.01	-0.07	0.16	-0.04	-0.04	0.23	0.19	0.4	0.2	0.18
Tombaugh 2	-0.24	1.62	15.76	-0.03	-0.06	-0.14	0.0	-0.27	0.2	0.09	0.14	0.24	0.03
Trumpler 20	0.13	1.86	7.18	0.21	0.17	0.12	0.18	0.15	0.07	0.06	-0.0	0.04	0.02
Trumpler 23	0.2	0.71	6.27	0.2	0.19	0.17	0.17	0.19	-0.0	-0.01	-0.02	-0.04	-0.02
Trumpler 5	-0.35	4.27	11.21	-0.21	-0.3	-0.24	-0.19	-0.24	0.14	0.05	0.11	0.17	0.11

2

² [Fe/H] are from Randich et al. (2022), except clusters not present in that work for which it was calculated in this work. R_{GC} and age from Cantat-Gaudin et al. (2020).

Table A.2: WLS fitting coefficients of the relation $[s-/Fe] = m_1 \cdot \text{Age} + c$ for the Open Clusters in the three regions.

	$R_{GC} > 9$			$7 \leq R_{GC} \leq 9$			$R_{GC} < 7$		
	m_1	c	PCC	m_1	c	PCC	m_1	c	PCC
[Y II/Fe]	-0.016±0.007	0.169±0.021	-0.38	-0.034±0.012	0.153±0.019	-0.57	-0.016±0.017	0.025±0.027	-0.29
[Zr I/Fe]	-0.014±0.007	0.126±0.019	-0.40	-0.019±0.009	0.090±0.015	-0.52	-0.036±0.018	0.055±0.027	-0.55
[Ba II/Fe]	-0.043±0.006	0.266±0.019	-0.83	-0.033±0.014	0.141±0.033	-0.48	-0.104±0.031	0.130±0.048	-0.73
[La II/Fe]	-0.021±0.006	0.228±0.017	-0.65	-0.032±0.013	0.162±0.026	-0.57	-0.061±0.027	0.061±0.024	-0.61
[Ce II/Fe]	-0.020±0.003	0.191±0.007	-0.80	-0.036±0.012	0.145±0.024	-0.62	-0.057±0.027	0.110±0.032	-0.57

Table A.3: Weighted multilinear regressions of 3 variables fitting coefficients of the relation $[s-/α] = m_1 \cdot \text{Age} + m_2 \cdot R_{GC} + m_3 \cdot [Fe/H] + c$ for the Open Clusters in every region and the coefficients of the inverted stellar dating relation $\text{Age} = m'_1 \cdot [s-/α] + m'_2 \cdot R_{GC} + m'_3 \cdot [Fe/H] + c'$

	$R_{GC} > 9 \text{ kpc}$									
[s-/α]	$m_1 \pm \Delta m_1$	$m_2 \pm \Delta m_2$	$m_3 \pm \Delta m_3$	$c \pm \Delta c$	R^2_{adj}	c'	m'_1	m'_2	m'_3	
[Y/Mg]	-0.036±0.007	-0.005±0.006	0.179±0.103	0.319±0.076	0.61	8.861	-27.778	-0.139	4.972	
[Y/Al]	-0.033±0.007	-0.005±0.006	0.320±0.115	0.338±0.076	0.59	10.242	-30.303	-0.152	9.697	
[Y/Si]	-0.025±0.009	0.004±0.006	0.176±0.121	0.180±0.081	0.37	7.2	-40.0	0.16	7.04	
[Y/Ca]	-0.015±0.008	0.016±0.005	0.352±0.129	-0.003±0.068	0.51	-0.2	-66.667	1.067	23.467	
[Y/Ti]	-0.042±0.007	-0.001±0.007	0.142±0.119	0.242±0.084	0.64	5.762	-23.81	-0.024	3.381	
[Ba/Mg]	-0.102±0.005	0.003±0.007	0.046±0.010	0.425±0.092	0.95	4.167	-9.804	0.029	0.451	
[Ba/Al]	-0.074±0.009	-0.013±0.007	-0.063±0.121	0.490±0.094	0.75	6.622	-13.514	-0.176	-0.851	
[Ba/Si]	-0.054±0.010	-0.020±0.007	-0.145±0.134	0.496±0.091	0.55	9.185	-18.519	-0.37	-2.685	
[Ba/Ca]	-0.055±0.006	0.021±0.000	0.002±0.000	-0.001±0.000	0.82	-0.018	-18.182	0.382	0.036	
[Ba/Ti]	-0.083±0.011	-0.028±0.008	-0.289±0.186	0.623±0.108	0.68	7.506	-12.048	-0.337	-3.482	
	$7 < R_{GC} < 9 \text{ kpc}$									
[Y/Mg]	-0.044±0.015	-0.019±0.034	0.256±0.314	0.379±0.272	0.32	8.614	-22.727	-0.432	5.818	
[Y/Al]	-0.051±0.014	0.025±0.001	0.002±0.000	0.004±0.000	0.42	0.078	-19.608	0.49	0.039	
[Y/Si]	-0.023±0.010	0.015±0.003	-0.001±0.000	0.002±0.000	0.18	0.087	-43.478	0.652	-0.043	
[Y/Ca]	-0.022±0.011	-0.034±0.026	-0.214±0.163	0.402±0.213	0.18	18.273	-45.455	-1.545	-9.727	
[Y/Ti]	-0.022±0.016	-0.001±0.038	0.191±0.295	0.162±0.304	-0.03	7.364	-45.455	-0.045	8.682	
[Ba/Mg]	-0.035±0.015	-0.050±0.043	-0.436±0.414	0.594±0.343	0.38	16.971	-28.571	-1.429	-12.457	
[Ba/Al]	-0.053±0.028	-0.157±0.074	-1.429±0.530	1.596±0.573	0.57	30.113	-18.868	-2.962	-26.962	
[Ba/Si]	-0.036±0.020	-0.104±0.053	-1.039±0.419	1.060±0.410	0.56	29.444	-27.778	-2.889	-28.861	
[Ba/Ca]	-0.028±0.013	-0.070±0.032	-0.479±0.273	0.716±0.258	0.46	25.571	-35.714	-2.5	-17.107	
[Ba/Ti]	-0.032±0.017	-0.094±0.045	-0.863±0.329	0.983±0.353	0.45	30.719	-31.25	-2.938	-26.969	
	$R_{GC} < 7 \text{ kpc}$									
[Y/Mg]	-0.015±0.074	0.191±0.115	0.641±0.786	-1.365±0.789	0.25	-91.0	-66.667	12.733	42.733	
[Y/Al]	-0.103±0.066	0.050±0.100	0.780±0.726	-0.307±0.683	0.12	-2.981	-9.709	0.485	7.573	
[Y/Si]	-0.015±0.056	0.133±0.082	0.011±0.620	-0.865±0.567	0.12	-57.667	-66.667	8.867	0.733	
[Y/Ca]	-0.024±0.037	0.108±0.067	0.194±0.355	-0.637±0.450	-0.01	-26.542	-41.667	4.5	8.083	
[Y/Ti]	-0.070±0.064	0.114±0.107	0.297±0.654	-0.609±0.711	-0.04	-8.7	-14.286	1.629	4.243	
[Ba/Mg]	-0.031±0.033	0.254±0.041	-0.173±0.279	-1.606±0.253	0.76	-51.806	-32.258	8.161	-5.581	
[Ba/Al]	-0.151±0.035	0.169±0.043	0.507±0.367	-0.976±0.299	0.84	-6.464	-6.623	1.119	3.358	
[Ba/Si]	-0.053±0.029	0.235±0.042	-0.403±0.287	-1.406±0.277	0.89	-26.528	-18.868	4.434	-7.604	
[Ba/Ca]	-0.009±0.043	0.111±0.056	-0.686±0.307	-0.517±0.354	0.76	-57.444	-111.111	12.333	-76.222	
[Ba/Ti]	-0.137±0.029	0.237±0.049	0.239±0.307	-1.333±0.330	0.88	-9.73	-7.299	1.73	1.745	
	global									
[Y/Mg]	-0.036±0.011	0.006±0.010	-0.166±0.122	0.129±0.079	0.16	3.583	-27.778	0.167	-4.611	
[Y/Al]	-0.039±0.007	-0.001±0.005	-0.190±0.060	0.191±0.032	0.54	4.897	-25.641	-0.026	-4.872	
[Y/Si]	-0.026±0.006	0.010±0.005	-0.125±0.062	0.035±0.032	0.34	1.346	-38.462	0.385	-4.808	
[Y/Ca]	-0.019±0.006	0.012±0.004	0.075±0.068	0.003±0.038	0.29	0.158	-52.632	0.632	3.947	
[Y/Ti]	-0.035±0.007	0.006±0.007	0.054±0.086	0.114±0.060	0.40	3.257	-28.571	0.171	1.543	
[Ba/Mg]	-0.103±0.006	0.038±0.003	0.025±0.021	0.050±0.046	0.86	0.485	-9.709	0.369	0.243	
[Ba/Al]	-0.089±0.012	-0.014±0.009	-0.603±0.134	0.448±0.083	0.55	5.034	-11.236	-0.157	-6.775	
[Ba/Si]	-0.061±0.009	-0.013±0.007	-0.536±0.112	0.340±0.068	0.51	5.574	-16.393	-0.213	-8.787	
[Ba/Ca]	-0.055±0.005	0.020±0.002	0.009±0.014	0.015±0.030	0.84	0.273	-18.182	0.364	0.164	
[Ba/Ti]	-0.066±0.008	-0.017±0.008	-0.477±0.102	0.397±0.076	0.56	6.015	-15.152	-0.258	-7.227	